Electromagnetic Metamaterials for Controlling Absorption and Thermal Emission

By

Zachary J. Coppens

Dissertation

Submitted to the Faculty of the

Graduate School of

Vanderbilt University in partial

fulfillment of the requirements

for the degree of

DOCTOR OF PHILOSOPHY

in

Mechanical Engineering

December 16, 2017

Nashville, Tennessee

Approved:

Jason G. Valentine, Ph.D.

Richard F. Haglund, Ph.D.

Deyu Li, Ph.D.

Cary L. Pint, Ph.D.

D. Greg Walker, Ph.D.

To my beloved family

ACKNOWLEDGEMENTS

I would like to take this opportunity to thank all those whose support and guidance made this dissertation possible.

First and foremost, I want to thank my Ph.D. advisor, Dr. Jason Valentine. His constant encouragement and demand for perfection allowed me to develop as an independent researcher. Dr. Valentine taught me many things, but none more important than how to think critically, a skill that will propel me throughout my career. I am forever grateful for Dr. Valentine's mentorship and will always consider him a friend.

I would also like to thank my committee members - Dr. Richard Haglund, Dr. Deyu Li, Dr. Cary Pint, and Dr. Greg Walker. Their valuable feedback on research and advice on career options have been greatly appreciated. I especially want to thank Dr. Greg Walker who served as co-advisor during my Mater's studies. I have had many memorable discussions with Dr. Walker on subjects ranging from heat transfer to life advice.

I next want to thank my labmates - Parik Moitra, Wenyi Wang, Wei Li, Yuanmu Yang, Zhihua Zhu, Austin Howes, You Zhou, and Fabian Ugwu. They made graduate school a very enjoyable experience; I will always remember our stimulating discussions and fun adventures outside the lab. I would like to single out a few lab members who have made a particular impact on my graduate career. First is Parik Moitra who was the first member in the Valentine lab. Parik assisted me through all phases of research including simulation, fabrication, and characterization, which greatly helped me in the early stages of my graduate experience. Next is Wei Li with whom I collaborated on several projects. Wei and I spent many late hours together taking data, and I will always remember the joy we

experienced when we got our first project to work. Finally, I want to thank You Zhou for all the inspiring discussions on the current and future directions of the metamaterials field.

I want to thank all the VINSE staff including Dr. Tony Hmelo, Dr. Ben Schmidt, Dr. Bo Choi, Dr. Dmitry Koktysh, and Kurt Heinrich for training me on all the VINSE equipment and helping me solve fabrication and characterization issues. I also want to give a special thanks to all my friends in Nashville. The time spent with them playing sports, going to concerts, and experiencing the city made my graduate experience that much more enjoyable.

Finally and most importantly, I want to thank my family, especially my wife Katie. Thank you for going on this journey with me; I know it was not easy placing our lives on hold while I pursued my dreams. I could not have finished this process without your unwavering support and encouragement. Thank you for believing in me.

TABLE OF CONTENTS

Page

LIST OF TABLES

LIST OF FIGURES

Figure Page

LIST OF PUBLICATIONS

- Z. Coppens, A. Cohn, F. Ugwu, Z. Zhu, C. Pint, and J. Valentine, "Electrochemically Actuated Metasurface for Dynamic Color Generation", *in preparation*

- Z. Coppens and J. Valentine, "Spatial and Temporal Modulation of Thermal Emission", **Advanced Materials** 1701275 (2017).

- Z. Coppens, I. Kravchenko, and J. Valentine, "Lithography-Free Large-Area Metamaterials for Stable Thermophotovoltaic Energy Conversion", **Advanced Optical Materials** 4 (2016).

- W. Li, Z. Coppens, L. Vazquez, W. Wang, A. Govorov, and J. Valentine, "Circularly Polarized Light Detection with Hot Electrons in Chiral Plasmonic Metamaterials", **Nature Communications** 6 (2015).

- Z. Coppens, W. Li, D. G. Walker, and J. Valentine, "Probing and Controlling Photothermal Heat Generation in Plasmonic Nanostructures", **Nano Letters** 13 (2013).

- W. Li, Z. Coppens, D. G. Walker, and J. Valentine, "Electron beam physical vapor deposition of thin ruby films for remote temperature sensing", **Journal of Applied Physics** 16 (2013)

Chapter 1: Introduction

1.1 Motivation

Engineering the interaction between electromagnetic radiation and matter has led to some of the greatest advances in our society. These include, but are not limited to, high-speed communication and data transfer, efficient solar energy harvesting, remote optical sensing, and high-resolution imaging systems. As scientists and engineers push the frontiers of technology it becomes increasingly important to move beyond the limits of conventional materials and develop a new generation of materials with advanced optical properties and functionalities.

The complete, classical description of light-matter interaction is given by Maxwell's equations,

$$\begin{aligned} \nabla \cdot \boldsymbol{B} &= 0, \\ \nabla \times \boldsymbol{E} &= -\frac{\delta \boldsymbol{B}}{\delta t}, \\ \nabla \cdot \boldsymbol{D} &= \rho, \\ \nabla \times \boldsymbol{H} &= \boldsymbol{j} + \frac{\delta \boldsymbol{D}}{\delta t}, \end{aligned} \tag{1.1}$$

where $\boldsymbol{B}$ is the magnetic flux density, $\boldsymbol{D}$ is the electric flux density, $\boldsymbol{E}$ is the electric field, $\boldsymbol{H}$ is the magnetic field, ρ is the charge density, and $\boldsymbol{j}$ is the current density. The constitutive relations for the magnetic and electric flux densities are,

$$\boldsymbol{D} = \varepsilon_r \varepsilon_o \boldsymbol{E}$$
$$\boldsymbol{B} = \mu_r \mu_o \boldsymbol{H} \tag{1.2}$$

where ε_o is the permittivity of vacuum, μ_o is the permeability of vacuum, and ε_r and μ_r are the relative complex electric permittivity and magnetic permeability, respectively. From the relations, we see that the material dependent properties ε_r and μ_r dictate how the material responds to electromagnetic radiation. In bulk materials, ε_r and μ_r are governed by the atomic composition and arrangement of a crystal lattice. This means achieving arbitrary control of bulk optical properties requires atom-scale engineering, a level of precision not available with current technologies.

Though arbitrary atomic engineering is not currently possible, fabrication advances in the last several decades have allowed scientists and engineers to create precise features on the nanoscale. Using nanoscale features, it is possible to fabricate crystals of meta-atoms, where if the feature sizes are less than the wavelength of light, the crystal can be treated as an effective medium. An example of a meta-atom crystal is shown in Figure 1.1. The electric and magnetic properties of each meta-atom unit cell can be controlled through structuring which allows for the realization of arbitrary optical properties and even those not available in natural materials.

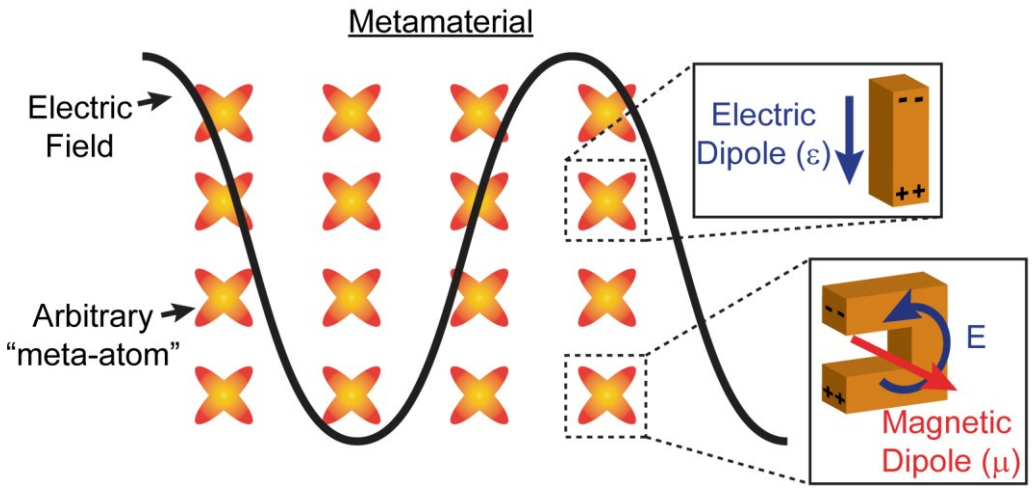

Figure 1.1. Schematic of metamaterial crystal. The black line represents an electromagnetic wave propagating through the crystal. The orange crosses represent unit cells in the metamaterial that can be of any arbitrary shape or material. Two unit cell examples are included in the right side of the figure. One is a metal bar that generates a strong electric dipole resonance that can be used to control permittivity (ε). The other is a metal split-ring resonator that generates a strong magnetic dipole resonance and can be used to control permeability (μ).

This engineered meta-atom crystal is known as a metamaterial, a term first used by Walser in 2001.[1] In its early stages, the metamaterial field became famous for demonstrations showing optical cloaking[2–5] and negative refractive index.[6–8] This exciting, initial work spurred the field and since then many studies have explored other metamaterial properties including epsilon-near-zero,[9, 10] engineered phase,[11, 12] and dynamic tunability.[13, 14] As the metamaterial field approaches the 20-year mark, its longevity will depend on how well scientists and engineers transition these advanced optical properties to practical devices. The goal of my work is to do just that. In the following dissertation, I highlight my development of metamaterial designs with enhanced absorption and thermal emission properties that solve technical engineering challenges in areas including energy conversion, heat transfer, and visible displays.

1.2 Absorption in Bulk Media

To appreciate the enhanced absorption metamaterial designs provide, we first explore absorption mechanisms in bulk media. The Lorentz oscillator model is used to describe light absorption in lossy, dielectric materials. In this model, the atoms are treated as mass spring systems with valence electrons attached to an atomic core by an imaginary spring (Figure 1.2a). The equation of motion for the electron is written as follows,

$$m(\ddot{x} + \gamma\dot{x} + \omega_o^2 x) = -q_e \boldsymbol{E} \tag{1.3}$$

where m is the mass, $\ddot{x}$ is the acceleration, γ is the damping rate, $\dot{x}$ is the velocity, ω_o is the natural frequency, and q_e is the electron charge. The damping term in the oscillator model causes energy loss in the material, producing a complex refractive index, $n = n_r - in_i$, where the imaginary part represents an attenuation of the wave. For a plane wave, this complex index causes the electric field to decay exponentially over a distance (z) in the material. The attenuation is graphically represented in Figure 1.2b. Because of the exponential decay, bulk materials can require large thicknesses to absorb all the incoming radiation.

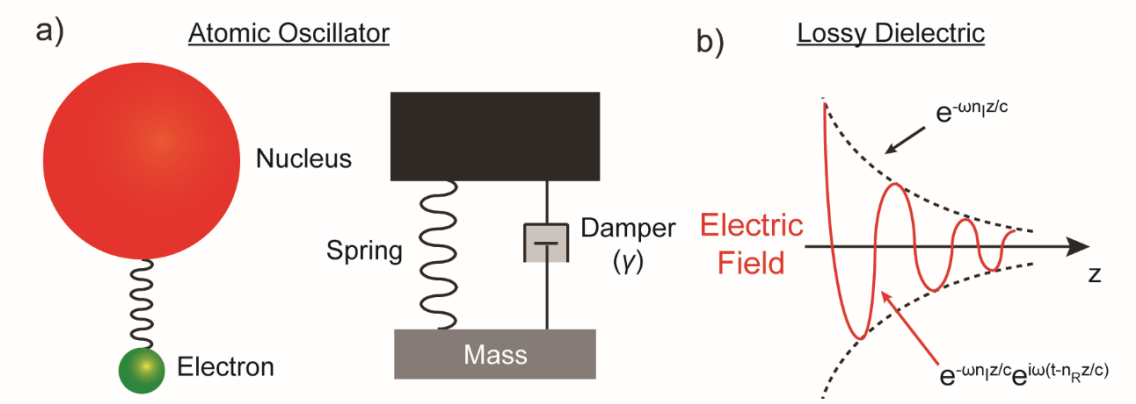

Figure 1.2. Absorption in a bulk, lossy dielectric. a) Lorentz oscillator model where the atom is modeled as mass-spring system. The damper in the model is responsible for energy absorption in the material. b) Plot showing absorption in a lossy dielectric. The damping term in the oscillator model causes the field to exponentially attenuate in the material. These figures are adapted from Fox[15] and Feynman.[16]

Another bulk absorption process includes interband transitions in semiconducting materials. In this process, electrons from the valence band can be excited to the conduction band by a photon with energy larger than the band gap. The excited electron will eventually decay back to the ground state through either radiative or non-radiative processes. If the electron decays non-radiatively, the photon energy is absorbed in the material. This interband absorption process will be used in Chapter 3 as a modulation mechanism.

Both of these bulk absorption mechanisms provide little spectral tunability as the spectral absorptivity is dictated by atomic structure, which cannot be easily manipulated. This means any spectral tuning is limited to mainly bulk material selection. The processes also provide little control of the polarization and spatial distribution of the absorbed energy. Furthermore, the absorptivity of bulk materials is difficult to tune dynamically.

These limitations can be overcome using engineered metamaterials.

1.3 Absorption in Metamaterials

1.3.1 Thermoplasmonics

One way to achieve metamaterial-enhanced absorption is using resonant plasmonic structures. A plasmon resonance occurs when an electromagnetic wave interacts with a metal nanoparticle causing the free electrons in the particle to coherently oscillate.[17] During the oscillations, resistance in the metal causes joule heating in the particle, which manifests as absorption. Typically, this absorption is considered a parasitic loss; however, in the growing research field of thermoplasmonics this loss is engineered to generate optically-induced nanoscale heat sources. Some potential applications in this area include chemical catalysis,[18] heat-assisted magnetic recording,[19] phononic circuitry,[20] and medical therapy.[21]

Initial work in the thermoplasmonic field explored the absorption properties of simple plasmonic geometries. In my first project, I wanted to see if more complex structures could be used to increase absorption and, consequently, the local heat generation. I found that nanostructures which create strong rotational magnetic fields produce enhanced absorption and heat generation, $q''' \propto H_\theta^2$. To find a structure with a large magnetic field hot spot, I used Babinet's principle, which states that the complementary structure of a material will provide a complementary optical response. Therefore, by taking the complimentary structure of a bowtie antenna, which produces an electric field hot spot (Figure 1.3a), I was

able to create a diabolo antenna, which provides a magnetic field hot spot (Figure 1.3b).[22] Comparing the diabolo antenna to a regular bar antenna, which has less magnetic field enhancement, I was able to experimentally validate the design rationale by showing that the diabolo antenna generates higher temperatures than the bar antenna (Figure 1.3c).

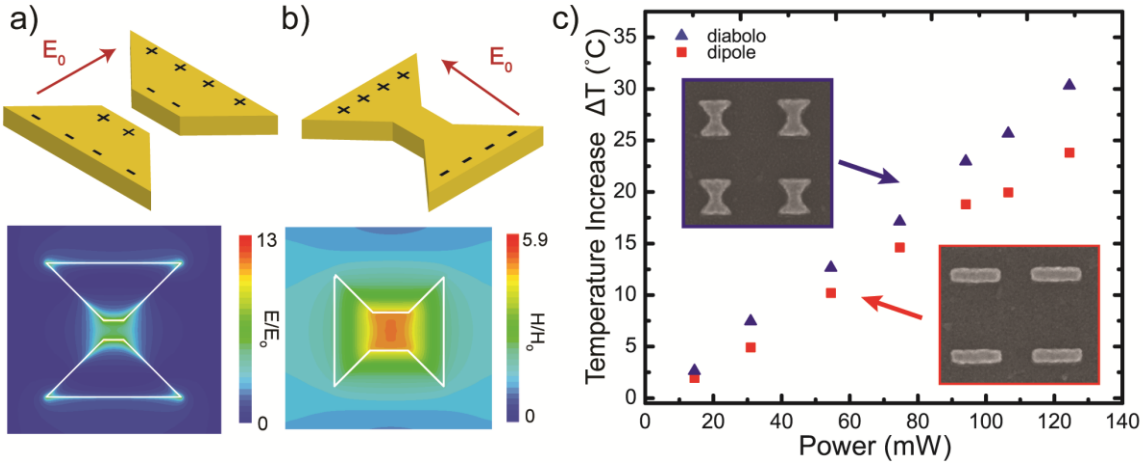

Figure 1.3. Absorption in thermoplasmonic metamaterials. a,b) Complementary antenna structures: bow-tie (a) and diabolo (b) with plots of the electric and magnetic fields, respectively. c) Temperature measurements of optically excited dipole (square) and diabolo (triangular) arrays versus heating beam power. ΔT is temperature rise over the ambient temperature. Insets show SEM images of the diabolo and dipole antenna. For reference, the dipole antenna length is roughly 200 nm.

Though this work demonstrated promising results, a major issue that hinders absorption in these plasmonic structures is scattering or re-radiation of energy back to the environment. In fact, the diabolo antenna achieved only 24% absorption at the resonant frequency. Therefore, for the rest of my work I wanted to study metamaterial geometries that could further improve absorptivity and potentially reach 100% absorption.

1.3.2 Metamaterial Perfect Absorber

When incident light reaches the surface of a material it can either be reflected, transmitted, or absorbed as shown in Figure 1.4a. Therefore, to create a metamaterial with 100% absorption, the transmission and reflection from the surface should be minimized. The transmission can be minimized by simply coating a substrate with a metal film. Minimizing reflection, however, requires impedance matching the material to free-space, which generally demands more complex structuring of meta-atoms. The equation for impedance matching is written as,

$$R = \left|\frac{Z_2 - Z_1}{Z_2 + Z_1}\right|^2 \qquad Z_2 = \sqrt{\frac{\mu_2}{\varepsilon_2}} \tag{1.4}$$

where R is reflection, Z_1 is the impedance of air, and Z_2 is the impedance of the material. If both Z_1 and Z_2 are equal then R is zero and the materials are said to be impedance matched. Because the impedance of free space is unity (Z_1=1), the matched impedance in the material occurs at the spectral position where μ_2 and ε_2 are equal.

The permittivity of a metamaterial is easily manipulated using metal nanostructures. Controlling the permeability, however, is more challenging because materials typically have a weak magnetic response in the optical regime. To create a metamaterial absorber with arbitrary control of permittivity and permeability, a metal resonator and dielectric spacer layer are added to a metal backplane as shown in Figure 1.4b. In this system, the top resonator acts as an electric dipole (Figure 1.4c) that controls the permittivity of the material. Meanwhile, a magnetic dipole is generated in the spacer layer (Figure 1.4d) due

to anti-parallel, circulating currents in the resonator and backplane. This gives the material artificial magnetic properties and control of the permeability. In this metamaterial architecture, permeability can be tuned by controlling the dielectric spacer thickness while the permittivity can be tuned by controlling the resonator length. At the spectral position where the permittivity and permeability match, the reflection is zero and, assuming loss in the system, the absorption will be 100% as shown in Figure 1.4e.

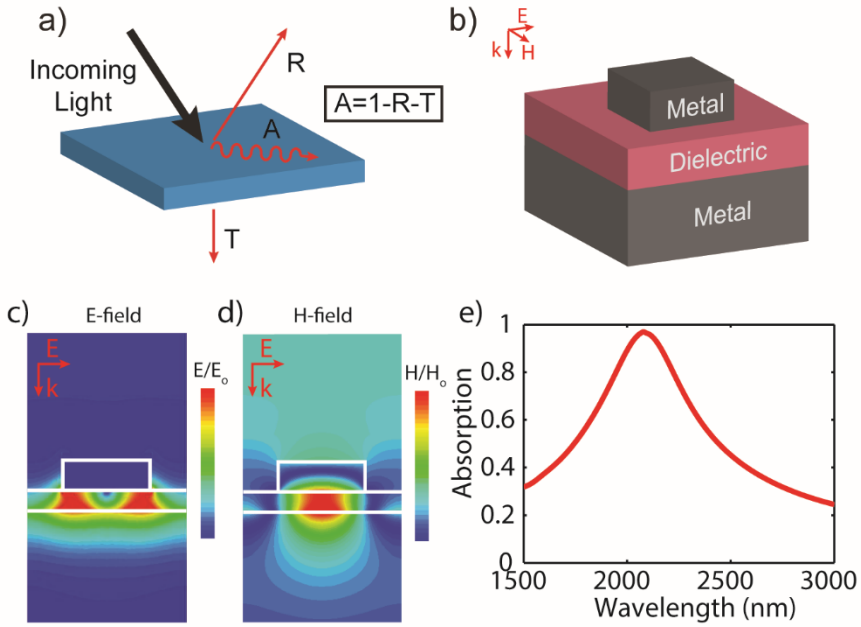

Figure 1.4. Designing a metamaterial perfect absorber. a) Schematic showing reflection, transmission, or absorption of incoming light. b) Metamaterial perfect absorber unit cell. c,d) Cross-sections taken through the middle of the unit cell showing the simulated electric field (c) and the magnetic field (d) distributions. Both fields are plotted at the resonant frequency of the metamaterial. e) Simulated spectral absorptivity of the metamaterial unit cell.

This metamaterial absorber design was first proposed in 2008 by Landy for a device in the GHz regime.[23] Since then, the design has been adapted to other frequency ranges

including the visible and infrared regime. The metamaterial absorber architecture offers many benefits over bulk absorbing materials. These benefits are highlighted in Table 1.1.

Table 1.1. Metamaterial Perfect Absorber Benefits

- Complete spectral control of the absorption peak
- Control over the absorbed polarization
- Omnidirectional or angle-selective response
- Localized field enhancements for improved interaction with surrounding media
- Ability for post-fabrication tuning of the resonance

Since 2008, several studies have explored how to utilize the benefits of the metamaterial perfect absorber geometry to solve practical engineering challenges. Some groups have tried to narrow the absorption peak for applications in sensing and absorption filters.[24–26] Other groups have explored designs that broaden the absorption peak to develop advance solar absorbing materials.[27–29] Currently, research has shifted to dynamic absorption control where the absorption properties are tuned dynamically.[30, 31] I believe this current focus on dynamic tunability is the most promising direction for the field.

1.4 Controlling Thermal Emission with Metamaterials

So far, I have discussed the metamaterial perfect absorber in terms of incoming photons being absorbed in a material. However, another interesting area of research for this metamaterial architecture is thermal radiation control where photons are thermally emitted from the material to free space. A material's thermal radiation characteristics are determined by its surface temperature and emissivity. Emissivity is a material property that

describes the fraction of emitted energy to that of a theoretical blackbody, which emits the maximum radiation allowed by quantum mechanics. We can use the metamaterial absorber architecture to control thermal emission because the absorptivity of a material is equal to its emissivity according to Kirchhoff's law. This means a perfect absorber is also a perfect thermal emitter.

Controlling thermal radiation is important because, of the three modes of heat transfer (conduction, convection, and radiation), thermal radiation offers the unique advantages of long-distance energy transfer and energy exchange without the need of an interacting medium. It also provides a significant source of infrared radiation that can be used to probe and control many interesting phenomena. Recent studies have explored the metamaterial absorber geometry as a thermal emitter for applications in energy management[32–37], sensing[38, 39], and infrared signature control.[40] However, there is still much more work to be done in this area.

1.5 Organization of the Dissertation

This dissertation is organized as follows:

Chapter 2 presents a large-area metamaterial thermal emitter that is fabricated using facile, lithography-free techniques. The device is composed of conductive oxides, refractory ceramics, and noble metals, and shows stable, selective emission after exposure to 1173 K for 22 h in inert and, for the first time, oxidizing atmospheres. The results of this chapter indicate that the metamaterial can be used to achieve high-performance thermophotovoltaic devices for applications such as portable power generation.

Chapter 3 presents another metamaterial perfect absorber geometry for thermal emission control; however, this time the emissivity of the material is dynamically modulated. The modulation is carried out using spatially patterned ultraviolet light that generates free carriers in a photosensitive ZnO spacer layer, causing a localized increase in emissivity. This work is the first demonstration of spatiotemporal emissivity modulation, an important advancement for thermal engineering applications such as smart, adaptive thermal management and rewritable infrared camouflage/displays. This material also achieves the largest integrated emissivity change among ultra-thin, low-power emissivity modulators.

Chapter 4 presents a metamaterial with selective absorption at visible frequencies for dynamic, reflective color generation. The metamaterial resonance is modulated using electrochemical actuation of a few-layer graphene spacer layer. The actuation operates at extremely low powers and can achieve high cycle stability. These attributes are important for displays in high-performance portable devices. In this chapter, I describe the theory behind the metamaterial design and present initial experiments demonstrating the color change. The results of this work could open opportunities for low-power, colored displays in electronic paper and digital signage.

Chapter 5 summarizes my work and highlights its long term implications. I also discuss future opportunities and challenges in the field.

Chapter 2: Lithography-free Large-area Metamaterials for Stable Thermophotovoltaic Energy Conversion

2.1 Introduction

In this chapter I explore the use of metamaterials for portable energy conversion applications. Common portable power devices include a range of battery technologies; however, batteries suffer from low energy densities which can cause unacceptable system-level weight additions. Combustible fuels, on the other hand, offer roughly two orders of magnitude increase in available energy density[41, 42], yet technologies to extract the power such as thermoelectric and thermionic generators suffer from low conversion efficiencies. As an alternative, thermophotovoltaic (TPV) generators, which use thermally emitted photons from a terrestrial source to power a photovoltaic cell, can provide significantly improved conversion efficiencies as well as high power density, fuel source flexibility, and robust and quiet operation.[41–45] TPV research has increased over the past decade due to recent advances in the development of nanostructured optical materials with much work being focused on designing ideal thermal emitters.

The ideal TPV thermal emitter must meet demanding spectral and mechanical design requirements. Spectrally, the emitter should produce an emissivity (ε) spectrum as follows: ε=1 for $E>E_g$ and ε=0 for $E<E_g$ where E is the energy of the thermally emitted photon and E_g is the bandgap energy of the photovoltaic cell. The step function at the bandgap ensures that all thermally emitted photons are capable of producing an electron-hole pair in the photovoltaic cell. This type of TPV emitter spectrum is desired for high

power density applications such as portable power generation and combined heat and power (CHP) as opposed to ultra-high-efficiency applications where the emitter spectrum should be quasi-monochromatic at the bandgap to reduce thermalization losses in the photovoltaic cell.[44, 46] In addition to being spectrally selective, the ideal emitter must also be polarization-independent and omni-directional. Mechanically, the emitter must not degrade when exposed to high-temperatures (>1100 K) and non-pristine atmospheres. High operational temperatures are required of TPV emitters so that the blackbody emission peak spectrally overlaps the bandgap of the photovoltaic cell.

Recent TPV emitters have included 1D-, 2D-, and 3D- photonic crystal[47–52] and metamaterial[27, 28, 36, 37] designs. Though these designs have generated much improvement toward the goal of stable and selective thermal emission, they typically possess shortcomings that can include material delamination, corrosion/oxidation, surface diffusion, and non-ideal spectral/angular emission profiles. Additionally, many of these designs require nanoscale fabrication techniques that are challenging, or expensive, to scale to practical device sizes. In this chapter, I present the design and experimental characterization of a metamaterial-based emitter that meets the demanding TPV spectral and mechanical requirements by using a combination of conductive oxides, refractory ceramics, and chemically inert metals. I show that the metamaterial can maintain spectral selectivity after exposure to both high-temperatures (1173 K) and oxidizing environments. The metamaterial is fabricated using large-scale, facile fabrication techniques which makes it practical for high-performance TPV portable power generators.

2.2 Design Methodology

The metamaterial metal-dielectric-metal perfect absorber geometry is used as the unit cell for the TPV emitter in this study. This geometry minimizes transmission with a metal backplane and minimizes reflection with resonant impedance matching to produce a condition of perfect absorption at a particular frequency.[25, 26] As mentioned in Chapter 1, this perfect absorption condition also translates into unity emission according to Kirchhoff's law.[33] Traditional gold and silver metal-dielectric-metal metamaterials will not survive the harsh TPV environments[27, 53], and therefore, special care must be taken in the selection of the constituent materials. In our design, we use indium tin oxide (ITO) as the backplane, gold disks as the top resonators, and aluminum oxide as both a spacer and encapsulation layer.

Figure 2.1a shows the metamaterial unit cell and Figure 2.1b displays the emissivity spectrum of the metamaterial as simulated using ITO optical properties taken from measured data (Table A.1) and gold properties taken from Johnson and Christy.[54] The spacer thickness and resonator diameter were chosen such that the emission peak lies below 2.5 μm (~0.5 eV), which is near the band-gap energy of a GaInAsSb TPV photovoltaic cell.[55] An electric field plot (Figure 2.1c) shows electric dipole coupling between the gold resonator and ITO backplane and a magnetic field plot (Figure 2.1d) reveals a magnetic dipole in the dielectric spacer layer. Both of these features confirm the resonant metamaterial perfect absorber response.[25] The power density plot in Figure 2.1e illustrates that most of the energy is absorbed in the ITO backplane. The optical penetration and subsequent absorption in the backplane is to be expected due to the low permittivity value of the ITO near the metamaterial resonant frequency.[27]

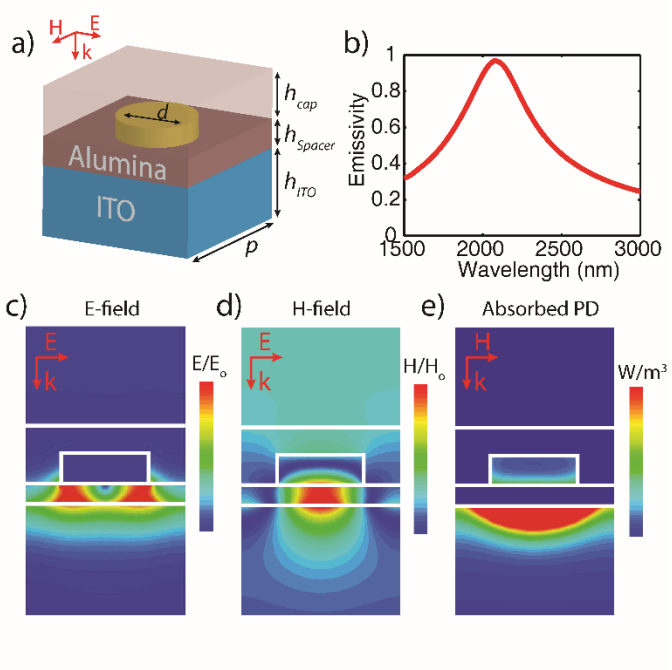

Figure 2.1 Metamaterial emitter design. (a) Unit cell where p= 250 nm, hITO= 400 nm, hspacer= 30 nm, hcap= 90 nm, and d= 140 nm. (b) Simulated spectral emissivity of metamaterial unit cell. (c-e) Cross-sections taken through the middle of the unit cell showing the (c) electric field, (d) magnetic field, and (e) absorbed power density (PD) distribution. All fields are plotted at the resonant frequency (2.1 μm) of the metamaterial.

Though ITO is generally thought of as a transparent conductor in electronics and photovoltaics, it has recently been studied as a high-performance plasmonic material in the near-infrared (NIR) and much effort has been expended to explore its unique plasmonic properties.[56–58] With proper deposition conditions and tin doping levels, ITO becomes metallic in the NIR (Figure A.1) and the material has demonstrated enhanced thermal stability at 1673 K in harsh environments through its use in high-temperature strain gauges.[59–61] These optical and mechanical features make ITO a superior choice for high-temperature, NIR thermal emitters. Gold is used in the design because of its chemical inertness and an encapsulation layer is added to maintain the shape of the gold at elevated

temperatures.[62, 63]

2.3 Fabrication of Metamaterial

To fabricate the metamaterial, 400 nm of ITO is first radio-frequency sputtered onto a cleaned sapphire substrate. The ITO was deposited in a 2 mTorr argon-only atmosphere and the substrate temperature was maintained at 623 K. Next, the gold resonators were fabricated using a dewetting process which takes advantage of the high surface energy and mobility of a gold film at elevated temperatures to create nanoislands.[64–66] To perform the dewetting process, 30 nm of aluminum oxide (spacer layer) was electron-beam deposited on top of the ITO followed by a 15 nm gold layer. The device was then heated to 1020 K for 15 min in an argon atmosphere to create the nanoisland resonators. The resulting metasurface contains a distribution of particle diameters with the mean diameter being controlled with the initial gold thickness (see Figure A.2).[65] Finally, 90 nm of aluminum oxide is deposited via atomic layer deposition (ALD) over the top of the resonators to complete the device fabrication.

This fabrication method consists only of thin-film deposition and post-annealing which provides a simple means to creating large-area metamaterials. Because the fabrication scheme does not use lithography, this metamaterial could be easily fabricated on a number of geometrically relevant TPV substrates including cylinders and hemispheres. Another advantage to the fabrication method is that the dewetting process provides a distribution of particle sizes which helps to broaden the resonance of the device compared to the single size resonator of traditional perfect absorbers.[66] The broader bandwidth will increase the power density of the device. Also, the dewetting process

allows the originally high surface energy gold film to naturally find a lower energy state which will help to maintain the resonator shape as the material is cycled back to higher temperatures.

Figure 2.2a shows the fabricated, large-area metamaterial (Sample 1). The uncoated, dewetted particles (Figure 2.2a, inset) have a distribution (Figure A.3a) with a mean diameter of 130 nm and a particle areal coverage of 20.0%. Both values closely resemble the dimensions of the unit cell simulation presented in Figure 2.1b that was conducted with a mean diameter and areal coverage of 140 nm and 24.6%, respectively. Another metamaterial emitter, Sample 2, was fabricated with an increased initial gold thickness (17 nm) which produced a metasurface with a mean diameter of 173 nm and coverage of 19.8% (Figure A.3b). Sample 2 was created to demonstrate the tunability of the design and to provide an additional sample for thermal stability testing.

Because a working TPV emitter includes an opaque back absorber, silicon carbide (634-SiC) is applied to the back surface of the sapphire substrate thus eliminating transmission and resulting in an emissivity that is given by $\varepsilon=\alpha=1-\rho$, where ε is emissivity, α is absorptivity, and ρ is reflectivity. Reflectivity measurements were performed with unpolarized light using a Varian Cary 5000 spectrophotometer and the measurements were calibrated with a gold mirror. The resulting emissivity curves of the two fabricated devices are shown in Figure 2.2b. As expected, the spectral position of the Sample 1 emissivity peak is similar to the simulated result and the emissivity spectrum has been advantageously broaden due to the distribution in resonator sizes (Figure A.4). Sample 2 experiences an expected red-shift in the emissivity profile due to the larger mean diameter of the metasurface and also shows an improved peak emissivity value when compared to Sample

1. The ability to tune the emissivity peak allows for spectral alignment with various TPV photovoltaic bandgap energies, and with optimization of both the mean particle diameter and spacer layer thickness it is expected that the peak emissivity can reach near unity values.[66]

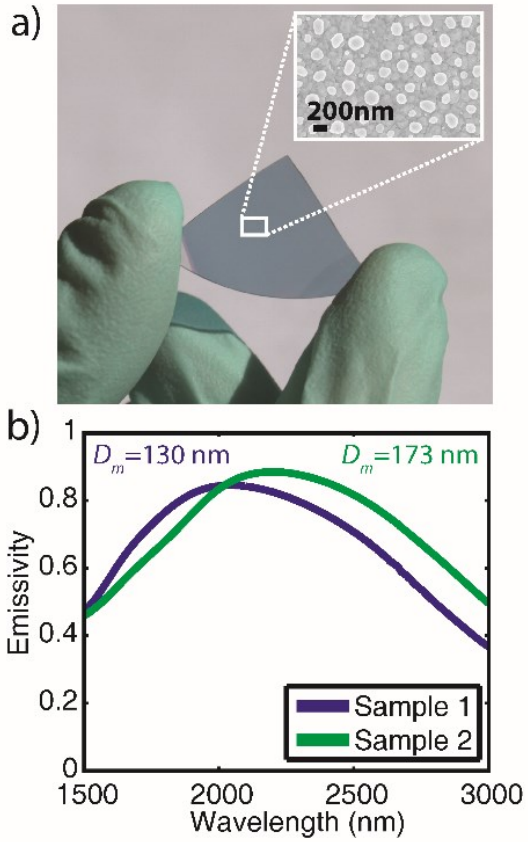

Figure 2.2. Metamaterial fabrication and characterization. (a) Fabricated metamaterial, Sample 1, pictured before application of silicon carbide back absorber and aluminum oxide encapsulation layer. Inset shows a SEM image of the dewetted gold resonators on top of the aluminum oxide spacer layer. (b) Measured spectral emissivity of Sample 1 and Sample 2 after adding the encapsulation layer. The mean resonator diameters (D_m) for each sample are 130 nm (Sample 1) and 173 nm (Sample 2).

2.4 Environmental Stability Testing

Next, the two samples were annealed at 1173 K in two different atmospheres to test the thermal stability of the design. The annealings were done in a 1 in. diameter evacuated quartz tube furnace (Lindberg/Blue M^{TM}) back filled with an atmospheric oxygen/argon ratio of either 2.3% (Sample 1) or 0% (Sample 2). Though the expected operational atmospheres of TPV devices will contain low oxygen concentrations, the introduction of oxygen to the Sample 1 experimental atmosphere was used to accelerate any possible oxidation damage. The annealing condition without oxygen (Sample 2) represents a more realistic operational environment and contains no gettering devices such as forming gas, tungsten foil, or carbon felt. During the annealing, the pressure was maintained near 5 torr which provides a balance between material evaporation and convection/conduction losses in an operational TPV system. The annealing pressure is also similar to what is found in commercially available tungsten filament light bulbs.[67]

The samples were annealed at increasing time intervals and the room temperature emissivity was measured after each annealing process. The spectral emissivities for Sample 1 and Sample 2 are shown in Figure 2.3a and Figure 2.3b, respectively. The results indicate that oxygen in the atmosphere does play a role in device performance as the emissivity profile of Sample 1 red-shifts with increased annealing time, eventually stabilizing after 14 hrs, while the spectral emissivity of Sample 2 remains largely unchanged.

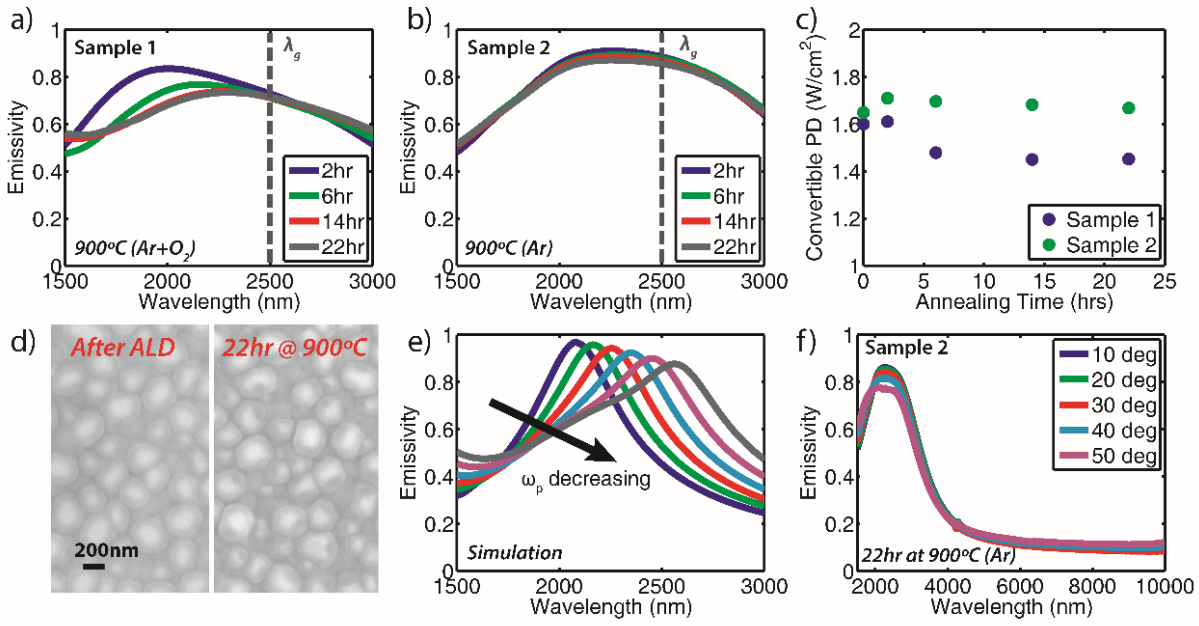

Figure 2.3. Metamaterial thermal stability demonstration. (a,b) Measured room temperature spectral emissivity of Sample 1(a) and Sample 2 (b) at different time intervals after annealing at 1173 K in Ar/O_2 (a) and Ar-only (b) atmospheres. λ_g corresponds to the bandgap energy of a GaInAsSb photovoltaic cell.[55] (c) Maximum convertible power density (PD) emitted from Sample 1 and Sample 2 as a function of annealing time. This calculation assumes a photovoltaic bandgap at 2.5 μm and an emitter temperature of 1173 K. (d) SEM images of Sample 1 taken after ALD of the Al_2O_3 encapsulation layer (left) and after 22 hr of annealing at 1173 K in Ar/O_2 (right). (e) Simulated spectral emissivity of metamaterial unit cell showing the result of a decreasing (or red-shifting) plasma frequency (ω_p) in the ITO backplane. (f) Angle-resolved spectral emissivity of Sample 2 after annealing 22 hr at 1173 K in an Ar-only atmosphere.

An important performance metric for any TPV emitter is convertible emitted power density, Q (W cm^{-2}). Q is calculated for Samples 1 and 2 at each annealing time interval using Equation (2.1),

$$Q(\lambda,T) = \int_0^{\lambda_g} \frac{\lambda}{\lambda_g}\varepsilon(\lambda)\frac{2\pi h {c_o}^2}{\lambda^5\left[exp\left(\frac{hc_o}{\lambda k_B T}\right)-1\right]}d\lambda \qquad (2.1)$$

where λ_g is 2.5 μm, λ is the emitted wavelength, ε is the measured emissivity, h is the

Planck constant, c_o is the speed of light in vacuum, k_b is Boltzmann's constant, and T is 1173 K. This equation assumes a perfect photovoltaic cell as described by Shockley and Queisser and represents an upper limit to the convertible power emitted by the metamaterial.[68, 69] The calculated power densities of both samples at each time interval are shown in Figure 2.3c demonstrating an initial decease in the power density from Sample 1 while Sample 2 remains nearly constant for the annealing times tested.

The fact that Sample 2 maintains its performance throughout the annealing process indicates that the red-shifting spectral emissivity in Sample 1 does not result from a catastrophic process. This is confirmed by the SEM images of Sample 1 before and after annealing (Figure 2.3d) which show no gross degradation. Instead, the red-shifting can be explained by a decrease in the free carrier concentration (n_e) of the ITO backplane. It has been shown that annealing ITO in oxygen-containing environments causes two carrier-reducing effects: the creation of neutralizing tin-oxygen defects and the reduction of oxygen vacancies in the indium oxide lattice.[70, 71] After prolonged annealing times the effects saturate and the number of carriers remains constant.[70] A decrease in n_e will decrease, or red-shift, the plasma frequency (ω_p) according to, $\omega_p{}^2 = \frac{n_e e^2}{\varepsilon_o m^*}$, where e is the electron charge, ε_o is the permittivity of free space, and m^* is the effective mass of the electron. Using the unit cell simulation from Figure 1, it is demonstrated that as the plasma frequency of the ITO backplane is red-shifted, the resulting spectral emissivity is also red-shifted (Figure 2.3e), matching the effect seen in the experimental results. Evidence of the saturation in carrier-reduction is seen in Figure 2.3c as the power density of Sample 1 after the 14 hr annealing time interval remains constant.

Both samples exhibit a large degree of spectral selectivity despite their exposure to

high temperatures, harsh environments, and repeated annealing. Though Sample 1 experiences an initial 9% decrease in convertible power density, the response saturates at longer time scales. The emitter does not suffer from enhanced oxidation and surface diffusion failures that have been observed in nanostructures composed of refractory metals[72] and noble metal thin films[73], respectively, and to the best of the authors' knowledge is the first experimental demonstration of an oxygen-tolerant nanostructured emitter. The spacer height and particle distribution of the metamaterial could also be optimized for the red-shifted ITO plasma frequency to maximize power output under these conditions. Sample 2, which was annealed in a more realistic environment, shows superior stability in its performance even without the aid of a reducing atmosphere. Figure 2.3f displays the angle-resolved room temperature emissivity of Sample 2 after 22 hours of annealing. The metamaterial retains a high emissivity over all angles near the design wavelength (2.5 μm) and a low emissivity at longer wavelengths which are both highly sought-after spectral features in TPV emitter design.

2.5 Theoretical TPV System Performance

To investigate how the metamaterial emitter might perform in a TPV system, Sample 2 was modeled in an idealized TPV configuration (Figure 2.4a). The idealized configuration provides an upper limit estimate of the system performance as it assumes a cold-side dielectric filter, a view factor of 1 between the emitter and photovoltaic cell, no parasitic conduction or convection losses from the emitter, and a perfect photovoltaic cell.[69] The cold-side dielectric filter, which is commonly used in TPV systems, provides a sharp cutoff in transmission at the bandgap of the photovoltaic cell so that photons emitted

with energies below the bandgap are reflected back to the emitter and thus recycled. This configuration is in contrast to recently proposed TPV systems that obtain sharp low-frequency cutoff through photonic bandgaps designed into the thermal emitter [48, 49]. For this study, a simple 5-layer quarter-wave stack of TiO_2/MgF_2 is simulated as the dielectric filter and its spectral reflectivity is displayed in Figure 2.4a. Details of the filter design are included in Figure A.5.

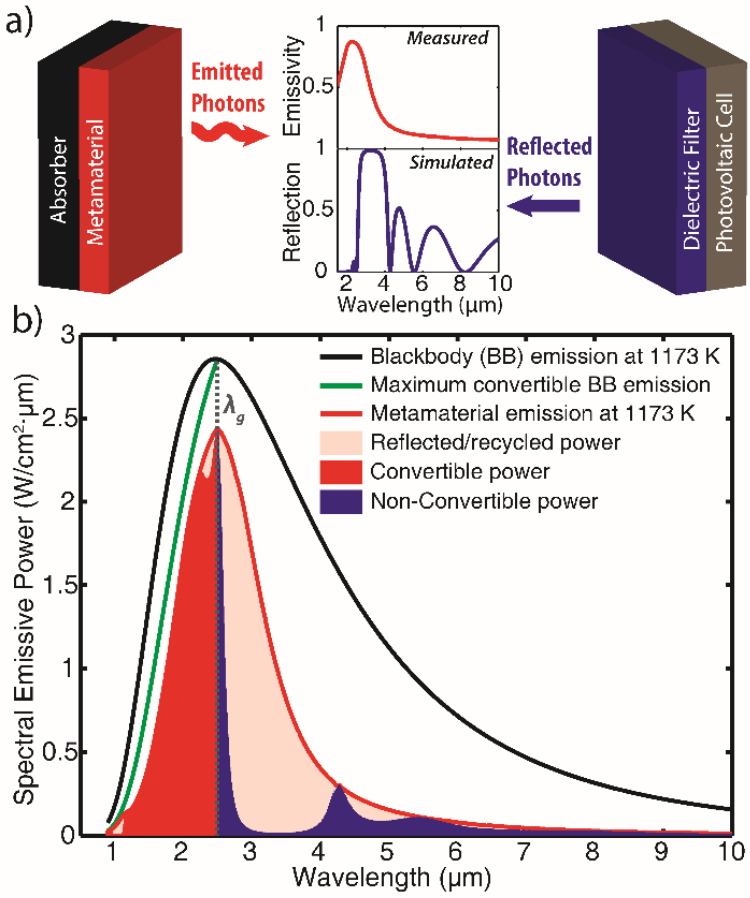

Figure 2.4. Modeled TPV performance. (a) Schematic of ideal TPV system including the measured spectral emissivity of Sample 2 after 22 hrs of annealing and the simulated spectral reflectivity of a quarter-wave TiO_2/MgF_2 cold-side filter. (b) Spectral emissive power of the metamaterial emitter when operating at 1173 K and in tandem with a cold-side, dielectric filter. λ_g corresponds to the bandgap energy of a GaInAsSb photovoltaic cell.[55]

The convertible and non-convertible spectral emissive power P (W cm^{-2} μm^{-2}) incident on the photovoltaic cell were calculated using Equation (2.2) based on the 22-hour annealed Sample 2 spectral emissivity (ε_m), the simulated filter spectral transmissivity (τ_f), and a temperature of 1173 K:

$$P(\lambda,T)=\begin{cases}\dfrac{\lambda}{\lambda_g}\varepsilon_m(\lambda)\tau_f(\lambda)\dfrac{2\pi h{c_o}^2}{\lambda^5\left[exp\left(\dfrac{hc_o}{\lambda k_B T}\right)-1\right]}, & \lambda\le\lambda_g\\ \varepsilon_m(\lambda)\tau_f(\lambda)\dfrac{2\pi h{c_o}^2}{\lambda^5\left[exp\left(\dfrac{hc_o}{\lambda k_B T}\right)-1\right]}, & \lambda>\lambda_g\end{cases} \tag{2.2}$$

The results of the model are displayed in Figure 2.4b. For reference, the blackbody curve at 1173 K (black) and the maximum convertible blackbody power (green) are included. The area under the red curve represents the emitted power from the metamaterial when heated to 1173 K. Due to the particle dispersion in the metamaterial, a portion of the emitted radiation falls below the bandgap energy (E_g) of the photovoltaic cell. With the cold-side filter, the amount of emitted power reaching the photovoltaic cell below the bandgap (blue area) is significantly reduced while the amount of convertible above bandgap power (red area) remains largely unchanged.

The emitter, cold-side filter tandem provides a significant performance advantage because the metamaterial strongly emits in the convertible spectral region while at the same time greatly suppressing non-convertible emission where the filter becomes transmissive (~4.2 μm). Evidence of this performance advantage is found when comparing the power spectral efficiency (η_{spect}) of the system with and without the filter, where η_{spect} is defined as the ratio of emitted power with photon energy above the bandgap to the total

emitted power incident on the photovoltaic cell. Without the filter η_{spect} of the system is 45.8% and with the filter η_{spect} increases to 75.3%. These values indicate that this initial metamaterial emitter design when used in a TPV system could provide significant performance advantages for portable power systems. It should be noted that these calculations were performed with idealized parameters and real systems will experience decreased performance due to losses as demonstrated in system-level studies that have achieved less than 5% overall efficiencies.[48, 49] However, optimization of the metamaterial design and incorporation of a more complex filter should improve the current performance (η_{spect}= 75.3%, Q= 1.63 W cm^{-2}), pushing it closer to that of an ideal TPV emitter (η_{spect}= 100%, Q= 2.16 W cm^{-2}). Ultimately, system-level demonstrations are needed to evaluate the true performance of these metamaterial-based emitters.

2.6 Conclusion

In this chapter I have demonstrated a metamaterial-enhanced thermophotovoltaic emitter that is capable of maintaining spectral selectivity after repeated long-duration, high-temperature (1173 K) exposures to oxidizing and inert atmospheres. The metamaterial is fabricated using facile, lithography-free processes that are scalable to practical emitter devices. The high-performance and thermal stability demonstrated in this study could allow TPV technology to become a viable portable power generation technology. This research is also beneficial to a number of energy conversion and high-temperature applications including selective IR light sources, high-temperature environmental sensing, and IR thermal regulation.

Chapter 3: Spatial and Temporal Modulation of Thermal Emission

3.1 Introduction

As demonstrated in the previous chapter, engineering thermal radiation requires the ability to precisely control the infrared optical properties of a material, most importantly the emissivity. While material selection provides some flexibility in dictating the emissivity, the use of structured materials offers far more freedom in controlling not only the spectral emissivity, but also the polarization and directional-dependence. In particular, metamaterials, which derive their properties from subwavelength structures,[23, 74, 75] have been used to engineer emissivity and thermal radiation over a wide parameter space for applications including energy harvesting,[27, 35, 76] chemical sensing,[39, 62] and heat management.[32, 47, 77] Recent work has extended emissivity control to spatially inhomogeneous[40] and dynamically reconfigurable materials.[78–81] However, to date, spatiotemporal control over emissivity has not been achieved.

In this chapter, I demonstrate simultaneous spatial and temporal control of emissivity using a metamaterial thermal emitter that is activated with spatially patterned ultraviolet (UV) light. The use of an all-optical modulation approach allows us to transfer the complexity associated with pixel-level control to the illumination source or an intermediate masking layer. Doing this dramatically reduces the nanophotonic material fabrication complexity and, when combined with a projection system, can allow emissivity control over large areas. Modulation is achieved through photocarrier doping of zinc oxide (ZnO) which increases optical losses in the metamaterial and causes a transition from low to high emissivity. Importantly, the ZnO layer has a long photocarrier lifetime allowing for

modulation of the metamaterial with low-power, continuous-wave illumination. The results from my work show that the metamaterial could be used to provide new capabilities for thermal engineering, especially in applications such as adaptive thermal management[34, 77] and rewritable infrared camouflage/displays.[82–85]

3.2 Metamaterial Design and Modulation Mechanism

The metamaterial architecture employed here is shown in Figure 3.1a and consists of gold resonators separated from an indium tin oxide (ITO) backplane by an n-doped ZnO film (n-ZnO). The metamaterial response can be understood using coupled mode theory, modeling the material as a one-port resonator (Figure 3.1b, inset). In this case, the emissivity at the resonant frequency is given by,

$$\varepsilon_{\omega_o} = 1 - r^2 = 1 - \left(\frac{\Gamma_r - \Gamma_i}{\Gamma_r + \Gamma_i}\right)^2 \tag{3.1}$$

where r is the complex reflection coefficient, Γ_r is the radiation loss, and Γ_i is the absorption loss.[86, 87]

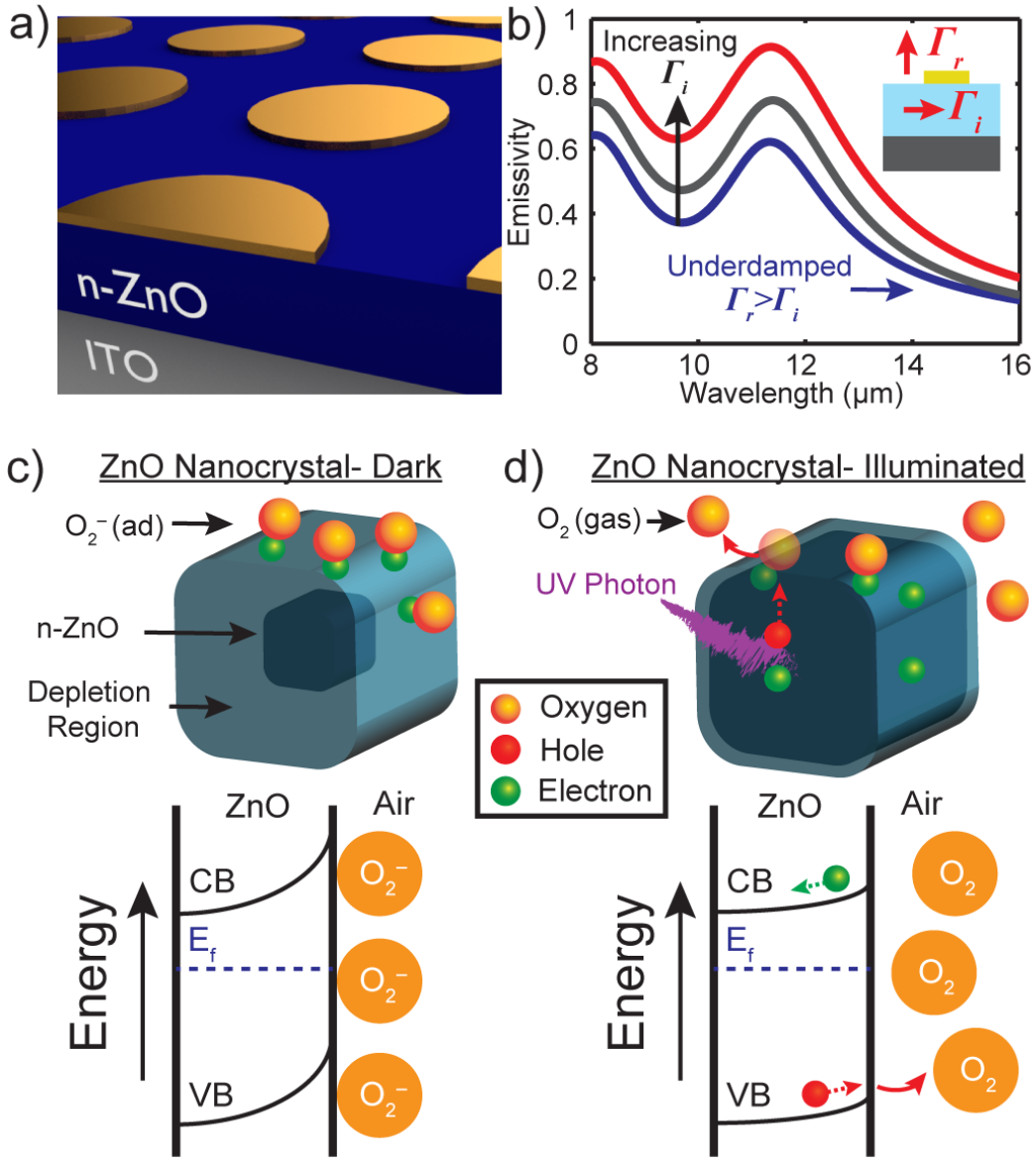

Figure 3.1. Active metamaterial emitter design and modulation mechanism. a) Metamaterial schematic with gold resonators, n-ZnO spacer layer, and ITO backplane. b) Simulated spectral emissivity with increasing absorption loss (Γ_i) in the metamaterial cavity. The absorption loss is increased by adding free carriers to the ZnO layer and the blue, grey, and red curves correspond to carrier concentrations of 3e17, 7e17, and 1.5e18 cm^{-3}, respectively. Inset shows a representation of the two loss mechanisms in the metamaterial (Γ_i and Γ_r). c) Schematic of ZnO nanocrystal under dark conditions with corresponding energy diagram. d) Schematic of ZnO nanocrystal after illumination from above bandgap photon with corresponding energy diagram.

Modulation of the emissivity is achieved by transitioning the metamaterial from an underdamped resonator ($\Gamma_r > \Gamma_i$ and $\varepsilon<1$) to a critically damped resonator ($\Gamma_r = \Gamma_i$ and $\varepsilon=1$) and vice versa. To make Γ_r greater than Γ_i and create an underdamped metamaterial, the n-ZnO spacer layer thickness can be increased to detune the coupling between the resonator and backplane (Appendix B.2). The underdamped condition is illustrated in Figure 3.1b (blue curve) which shows a peak emissivity less than unity when Γ_r is dominant. If absorption (Γ_i) is added, the emissivity will increase as the system approaches critical damping (Figure 3.1b). Increasing Γ_i past critical damping causes the system to become overdamped, resulting in a decrease of emissivity. Further details of the metamaterial simulations are included in Appendix B.2.

In the metamaterial employed here, modulation of Γ_i occurs in the ZnO layer due to photoinjected carriers that cause additional free carrier absorption and increased optical loss (Figure B.1d) according to the Lorentz-Drude model,

$$\varepsilon'(\omega) + i\varepsilon''(\omega) = \varepsilon_\infty \left[1 + \frac{\omega_{LO}^2 - \omega_{TO}^2}{\omega_{TO}^2 - \omega^2 - i\gamma\omega} - \frac{\omega_p^2}{\varepsilon_\infty \omega(\omega + i\Gamma)}\right] \tag{3.2}$$

where $\omega_p{}^2 = \frac{ne^2}{\varepsilon_o m^*}$, and n is the free carrier concentration. When the illumination source is removed, the photocarriers recombine and Γ_i and emissivity return to their original state. The photoactivated change in carrier concentration is described by,

$$\Delta n = \frac{\beta I \tau_{rec}}{L_D} \tag{3.3}$$

where β is quantum efficiency, I is illumination intensity, τ_{rec} is effective carrier lifetime, and L_D is diffusion length. In typical optically activated materials where the main goal is ultrafast modulation, the carrier recombination time of Equation (3.3) should be

minimized.[88, 89] However, low τ_{rec} requires a high input intensity (I) to change the carrier concentration which is not desirable for applications involving large-area modulation with modest illumination intensity. Here, we seek to lower the required modulation intensity, and therefore an active material with large τ_{rec} is desired.

Though single-crystal ZnO possesses picosecond to nanosecond recombination times,[90] polycrystalline ZnO can prolong carrier lifetime into the millisecond and second range due to hole trapping from interfacial oxygen adsorption.[91–94] This mechanism is outlined in Figure 3.1c and Figure 3.1d. In dark conditions, oxygen molecules adsorb to ZnO nanocrystallite boundaries and trap free electrons ($O_{2(g)} + e^- \rightarrow O^-_{2(ad)}$) resulting in a depletion region near the ZnO/air interface (Figure 3.1c). This built-in potential causes photogenerated electrons and holes to separate resulting in holes rising to the surface and desorption of the oxygen ions ($h^+ + O^-_{2(ad)} \rightarrow O_{2(g)}$) while the electrons travel to the bulk of the nanocrystal (Figure 3.1d). During illumination, the adsorption and desorption equilibrium state produces a net increase in the ZnO free carrier concentration which increases metamaterial emissivity. Once the illumination source is removed, oxygen readsorbs to the interface which traps the free carriers and causes the emissivity to return to its original dark state.

3.3 Metamaterial Fabrication and Characterization

To fabricate the photoactive metamaterial, 400 nm of ITO was first sputtered onto a sapphire substrate. ITO was chosen because it provides a reflective backplane in the infrared, while also providing transparency in the UV-Vis region of the spectrum.[35] This visible transparency allows for emissivity modulation using back-side illumination, a

potentially important feature in infrared signature control applications. Next, 950 nm of n-ZnO was sputtered onto the ITO film at 200 °C to create a nanocrystallite spacer layer. Finally, gold resonators were patterned on top of the n-ZnO layer using photolithography and lift-off followed by a 40 nm n-ZnO encapsulation layer that was deposited over the entire metamaterial. The encapsulation layer was included to improve UV absorption in the ZnO during top-side illumination and to extend the ZnO/Au interface, which increases photocarrier lifetime due to Schottky barrier hole trapping.[95]

An SEM image of the fabricated metamaterial is shown in Figure 3.2a. To characterize the metamaterial emissivity, the reflectivity (R) of the sample was measured in a Fourier Transform Infrared (FTIR) spectrometer and converted to spectral emissivity, $\varepsilon(\lambda) = 1 - R(\lambda) - T(\lambda)$, where $T(\lambda) = 0$ due to substrate opacity in the infrared. The resulting emissivity, displayed in Figure 3.2b (blue curve), shows an underdamped condition with a peak emissivity less than unity. The metamaterial emissivity was then measured under constant illumination from a UV LED source (0.4 $mWcm^{-2}$). The result in Figure 3.2b (red curve) shows an increase in peak emissivity of $\Delta\varepsilon \approx 0.16$ and a total integrated emissivity change of $\Delta\varepsilon_{int} \approx 0.12$. The integrated emissivity change is an important figure of merit for radiative heat transfer and infrared signature control applications because these applications rely on the total emitted flux to control cooling power and apparent temperature change, respectively. To the best of our knowledge this represents the largest integrated emissivity change for low-power, ultra-thin emissivity modulators. Past work has demonstrated much more modest integrated emissivity changes of $\Delta\varepsilon_{int} \approx 0.02$[79] and $\Delta\varepsilon_{int} \approx 0.002$[81]. Analysis presented in Appendix B.3 shows how the integrated emissivities were calculated.

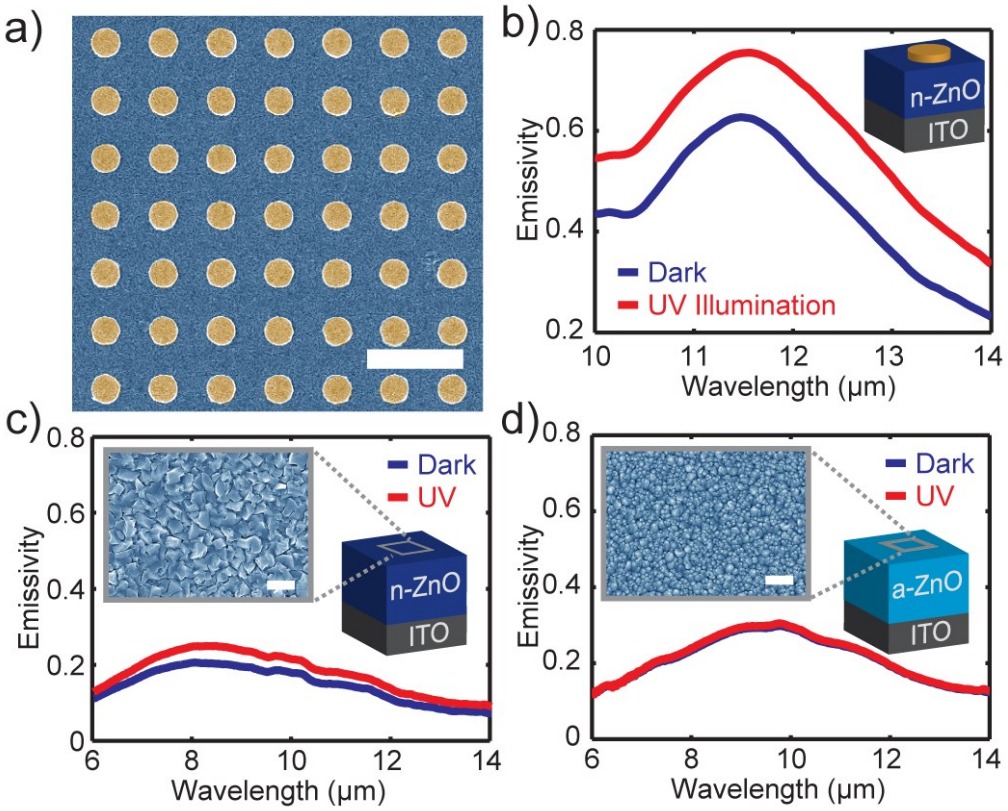

Figure 3.2. Metamaterial fabrication and characterization. a) SEM image (false color) of the gold resonators deposited on top of the n-ZnO layer. Scale bar is 10 μm. b) Measured spectral emissivity of the metamaterial before and after UV illumination. c,d) Measured spectral emissivity of c) n-type and d) amorphous ZnO films before and after UV illumination. Insets show unit cell schematics and SEM images (false color) of the fabricated photonic materials.

To better understand the nature of the emissivity modulation, two reference samples were fabricated consisting of only ITO and ZnO layers. These samples had no metamaterial layer and thus function simply as bilayer, anti-reflection absorbers.[96] The first sample was fabricated with the same deposition conditions as the metamaterial film and possessed a polycrystalline n-ZnO layer as seen in Figure 3.2c, inset. The purpose of this sample is to elucidate the role of the metamaterial response. For the second sample, the

ZnO layer was deposited on ITO at room temperature to create an amorphous layer (a-ZnO)[88] as shown in Figure 3.2d, inset. In comparison to n-ZnO, the a-ZnO layer has a large number of bulk defects that act as recombination sites for photogenerated electron-hole pairs causing a decrease in the effective free carrier lifetime.[97] For the same illumination intensities, Equation (3.3) predicts the a-ZnO film will have a smaller change in carrier concentration and consequently a smaller emissivity modulation.

Figure 3.2c and Figure 3.2d show the dark and UV illuminated spectral emissivity of both samples measured under the same conditions as the metamaterial emitter. The n-ZnO film possesses a much smaller change in emissivity compared to the metamaterial demonstrating the importance of the enhanced mode confinement within the n-ZnO layer (Appendix B.4). However, the n-ZnO film has a much larger change in emissivity compared to the a-ZnO film, demonstrating that emissivity modulation is indeed a result of photodoping in the ZnO and that a long free carrier lifetime is critical to low-intensity modulation. Using the same n-ZnO film, the effect of oxygen adsorption was explored by passivating the nanocrystal interfaces using a hydrogenation technique (Appendix B.4).[98, 99] This passivation reduced the change in emissivity, supporting the oxygen adsorption mechanism outlined in Figure 3.1.

3.4 Thermal Camera Measurements

To better understand the temporal and spatial emissivity response, the metamaterial was imaged using a FLIR A655sc thermal camera in the setup shown in Figure 3.3a. The thermal camera measures the total thermal radiance (M_{tot}) of an object and calculates an apparent temperature (T_{obj}) according to,

$M_{tot} = \varepsilon S(T_{obj}) + (1-\varepsilon)S(T_{amb}) - S(T_{camera})$, where S is the integrated blackbody flux in the spectral range of the camera.[83] When the emissivity input to the camera is held constant and the metamaterial thermal radiance (M_{tot}) is altered due to modulated emissivity, the displayed apparent temperature will fluctuate even though the temperature of the metamaterial is uniform. Therefore, monitoring the apparent metamaterial temperature before, during, and after UV illumination provides an indirect method to observe the dynamic emissivity modulation.

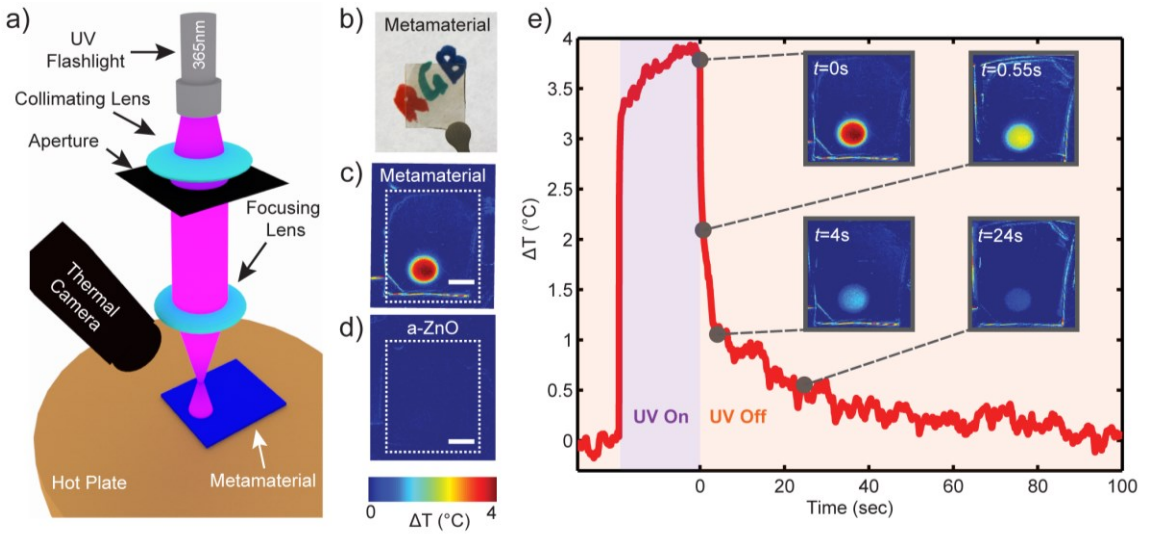

Figure 3.3. Demonstration of apparent temperature increase and temporal response of metamaterial. a) Thermal imaging setup including focused UV excitation from an LED flashlight. b) Optical image of metamaterial demonstrating visible transparency. c) Thermal image of metamaterial sample after illumination from UV source. d) Thermal image of a-ZnO film after illumination from UV source. The white dashed box in c) and d) outline the shape of both samples and the scale bar is 4 mm. e) Temporal response of metamaterial sample displaying the illuminated spot temperature as recorded by the thermal camera. t=0 is positioned on the x-axis at the moment UV illumination is removed. Each inset figure shares the same temperature and length scale bar as c) and d).

As an initial test, the metamaterial was placed on a heated copper plate and light from a UV LED source (10 $mWcm^{-2}$) was collimated and focused onto the top side of the sample. Heating the sample above the ambient temperature increases the contrast between the emitted flux, $\varepsilon S(T_{obj})$, and the reflected flux, $(1-\varepsilon)S(T_{amb})$, allowing for increased visibility of the emissivity change. Figure 3.3b shows an optical image of the metamaterial sample held over "RGB" colored letters to demonstrate optical transparency. After allowing the metamaterial to reach steady-state, the apparent temperature increase due to emissivity modulation was captured and displayed in Figure 3.3c. The image shows a significant change in the apparent temperature (ΔT=4 °C) only where the UV illumination source is projected on the sample indicating a highly localized increase in emissivity.

To ensure the apparent temperature change was not a result of photoinduced heating from the absorbed UV light, the a-ZnO film was imaged under the same experimental conditions as the metamaterial. This test allows for a direct measurement of the photoheating contribution to the apparent temperature change because the a-ZnO film absorbs virtually the same amount of UV energy as the metamaterial (Figure B.4a), but has a negligible emissivity change in the infrared spectrum (Figure 3.2d). Therefore, any apparent temperature rise measured from the a-ZnO film can be directly correlated to the photoheating contribution in the metamaterial. Note that though the metamaterial contains gold which has strong absorption in the UV, the a-ZnO film absorbs just as strongly in this spectral region (Figure B.4a), and therefore the gold will not induce any additional heating. Figure 3.3d shows the thermal image for the UV illuminated a-ZnO film. There is no discernible apparent temperature rise in the film which indicates that the apparent temperature change measured on the metamaterial is indeed a result of emissivity

modulation. In addition, calculations using a conservative thermal model show that for the experimental input intensity, a negligible temperature rise of 0.10 °C is expected (Appendix B.5).

3.5 Temporal Response

The temporal response of the active metamaterial emitter was explored by modulating the illumination source. Because the active layer was engineered to increase free carrier lifetime, it is expected that the recovery time should be relatively long. Figure 3.3e shows that the optically addressed area experiences a rapid increase in apparent temperature followed by a double exponential relaxation with a fast initial decay (0.645s) and a slower final decay (33.7s). The fast relaxation is attributed to the rapid recombination of free electrons and trapped holes as a result of the low initial interfacial barrier height.[100] After the initial recombination, the re-adsorbed oxygen molecules cause an increase in barrier height which reduces the recombination rate and slows the decay process. The initial emissivity is recovered in approximately 100 sec and the decay is visualized in the Figure 3.3e inset images. A multi-excitation plot is included in Appendix B.6. While the slower recovery of initial emissivity prevents use in high-speed applications, it is not detrimental to slower emissivity changes such as those used for infrared camouflage, identification tags, or thermal management.

3.6 Spatial Response

Due to the fact that emissivity change is confined to the photocarrier diffusion

length, pixilation of the metamaterial is not necessary and large-area spatial control can be achieved using a patterned illumination source. We can characterize the spatial resolution of the metamaterial emissivity modulator by using a projected Ronchi ruling as described in Appendix B.7. The material supports a 450 μm linewidth at a contrast ratio of 38%. This level of resolution is enough to distinguish details in projected macroscale images using the setup shown in Figure 3.4a. For the setup, projection masks were printed on transparencies and used to spatially redistribute UV light focused onto the metamaterial. Owing to the transparency of the substrate and ITO layer, the illumination source can be placed at the backside of the metamaterial which is demonstrated here to show the added utility of the material. During testing, the temperature of the metamaterial was held at 80 °C and all measurements were taken at steady-state.

Two different images were projected onto the metamaterial. The first is the Vanderbilt University anchor logo with the resulting thermal image displayed in Figure 3.4b. The figure shows clear temperature contrast between the illuminated and non-illuminated areas of the metamaterial which confirms the pixel-less spatial control of the emissivity modulation. Next, the UV illumination intensity was varied in one dimension using a grayscale mask. The thermal image in Figure 3.4c shows an apparent temperature gradient, which occurs because the change in carrier concentration and consequent change in emissivity is intensity dependent. This demonstrates that the emissivity modulation is not binary but can be tuned between high and low values to shape arbitrary 2D emissivity patterns. Though the current spatial resolution is adequate for the previous demonstration, applications requiring higher resolution could implement a spacer layer made of ZnO nanoparticles to drastically decrease photocarrier diffusion length by limiting charge

transport to particle hopping.[101]

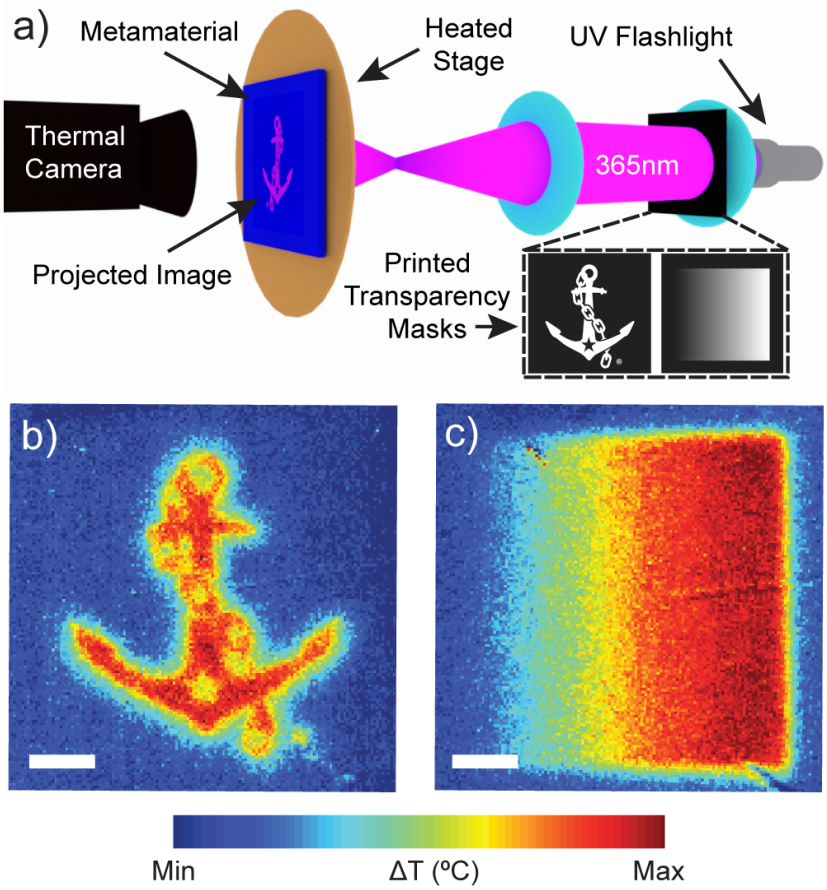

Figure 3.4. Demonstration of spatial emissivity control using UV projected images. a) Thermal imaging setup where UV images are projected through the backside of the metamaterial and thermal images are captured from the front side of the sample. Printed transparency masks were used to produce the thermal images in (b) and (c). b) Thermal image of Vanderbilt University anchor logo. c) Thermal image of grayscale block. The scale bar for (b) and (c) is 1 mm.

3.7 Conclusion

In conclusion, the simultaneous spatial and temporal emissivity modulation demonstrated in this work provides a new capability for thermal engineering devices. Our

dynamic metamaterial thermal emitter includes no complex electronic circuitry which allows for simple fabrication and implementation. Because the active layer is engineered to increase free carrier lifetime, the metamaterial emissivity can be modulated over large areas with modest continuous-wave illumination sources. The metamaterial has the largest integrated emissivity change among low-power, ultra-thin devices, and further engineering of the spacer layer carrier dynamics could easily improve both the dynamic range and spatial resolution for applications in next-generation advanced thermal materials.

Chapter 4: Electrochemically Actuated Metasurface for Dynamic Color Generation

4.1 Introduction

In the previous two chapters, I discussed how the metamaterial architecture could be used as a perfect emitter for thermal emission control. In this chapter, I will shift the response to the visible spectrum and instead use the metamaterial as an absorber for visible display applications.

As the power demands of portable electronic devices surge, it becomes increasingly important to lower display technology power consumption, as this component typically draws the most power in the system.[102] The lowest power consuming commercial displays are the electrophoretic and cholesteric liquid crystal display.[103] These displays operate using ambient reflection, which eliminates backlight power consumption, and are bi-stable meaning power is consumed only when the display is updated. Though these reflective display technologies have shown promise for low-power portable electronics devices, they have been limited to niche applications largely due to their relatively slow switching speeds and difficultly in producing colored images.[104]

An emerging area in reflective display technologies is structured color from subwavelength metasurfaces.[105–110] These materials offer advantages such as high-resolution pixels, phase and polarization control, and most importantly the ability to modulate color post-fabrication. Recently, groups have begun exploring bi-stable and dynamic color changes in metasurfaces using gasochromic[111] and reversible electrodeposition[112–114] modulation techniques. However, reversible electrodeposition

requires relatively high power consumption, gasochromics are impractical for portable devices, and both methods have slow switching speeds on the order of seconds and in some cases minutes.

In this chapter we show a metasurface design with bi-stable dynamic reflective color change spanning the full color gamut. The color is modulated using intercalation-induced actuation of a few-layer graphene (FLG) spacer layer, which changes the structure and resonant frequency of the metasurface. The intercalant ion is coated in a solvent shell, which provides enhanced modulation speed and cycle stability.[115] Results from this work could enable the next generation of low-power display technologies for applications including colored electronic paper and digital signage.

4.2 Metasurface Design and Working Mechanism

A unit cell of the metasurface is shown in Figure 4.1a and consists of an aluminum resonator separated from a silver backplane by a FLG spacer. We chose aluminum because of its ability to produce strong resonances in the blue part of the spectrum[116] and silver because of its low-loss reflection of visible light. As mentioned in previous chapters, this metasurface architecture provides perfect absorption at a designed wavelength[23, 33, 117, 118] which gives highly saturated colors in the CMYK subtractive color scheme.[116] The metasurface response is also polarization independent, providing high reflection efficiency, and omnidirectional, meaning the hue does not change with viewing angle.[25]

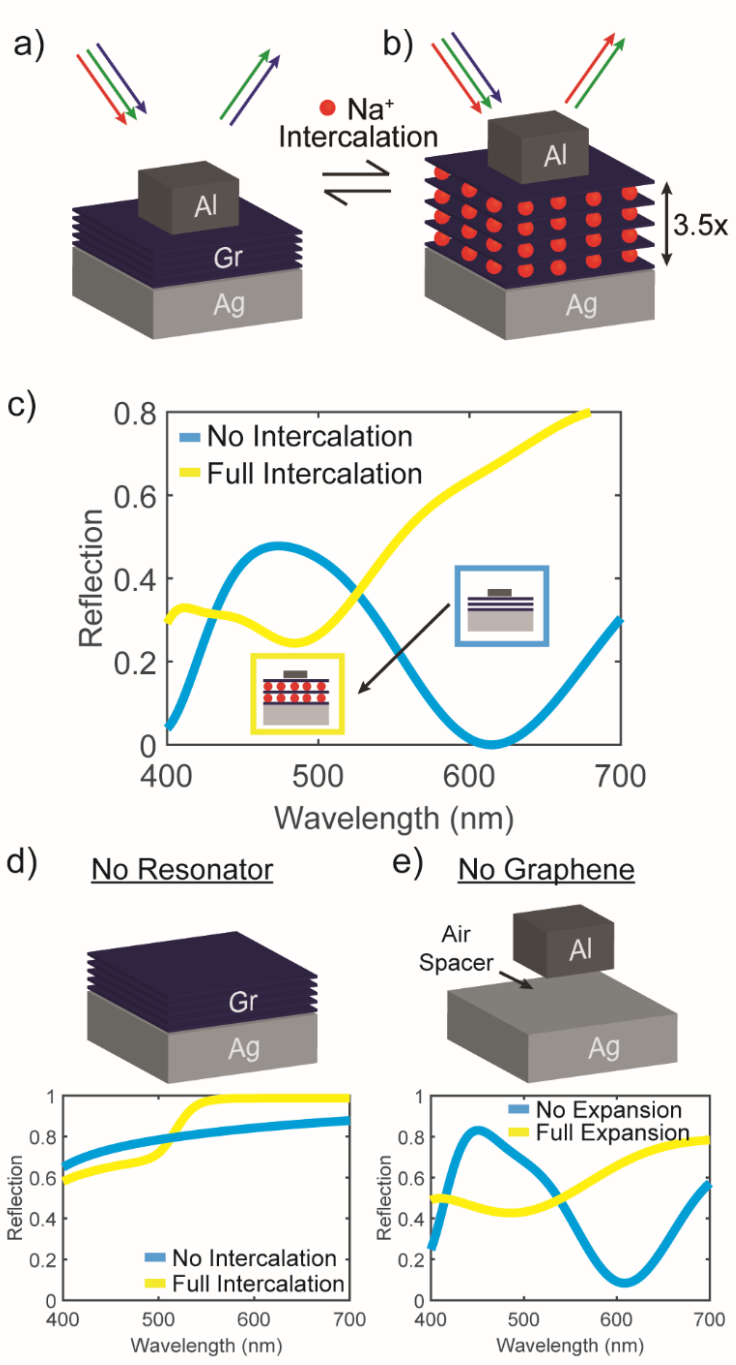

Figure 4.1. Metasurface design and working mechanism. a) Unit cell of the metasurface with an unintercalated few-layer graphene spacer. b) Intercalated metasurface unit cell showing a change in reflected color. c) Simulated spectral reflectivity for the unintercalated and fully intercalated metasurface unit cell. Intercalation of the spacer layer (18 graphene sheets) causes a blue-shift in the resonant frequency. d) Simulations for a metasurface unit cell without the aluminum resonator. e) Simulations for a metasurface unit cell without the few-layer graphene spacer.

The working principle for the dynamic color change is briefly outlined as follows. Solvated sodium ions are electrochemically inserted between the graphene layers which causes a nearly 3.5 times z-direction expansion of the graphene stack[115] as shown in Figure 4.1b. This vertical actuation changes the coupling between the top resonator and the backplane causing a blue-shift in the resonant frequency as shown in Figure 4.1c. This design achieves low-power modulation because an extremely small mass of carbon is used in the spacer layer and because the solvated ions provide low energy storage capacity.

To determine that the color change is indeed due to metasurface spacer-layer actuation and not changes in graphene optical properties, two different structures were simulated. In the first case, the resonator is removed leaving only graphene layers on the backplane. In the second case, the graphene is removed leaving the resonator hovering over the backplane. Figure 4.1d shows the graphene-only case which, in the fully intercalated state, provides improved red and green reflection. This well-known optical phenomenon in graphene intercalant compounds is attributed to Pauli blocking at visible frequencies.[119, 120] The simulation in Figure 4.1e, which contains no graphene, shows a blue-shift in the resonant frequency when the resonator is moved away from the backplane. This shift is similar to the full metasurface response in Figure 4.1c and indicates that the metasurface resonance shift is largely due to actuation of the spacer layer. It is importation to note, however, that Pauli blocking in the fully intercalated graphene works together with the resonance shift to boost yellow saturation.

4.3 Metasurface Fabrication and Characterization

To fabricate the metasurface, FLG was mechanically exfoliated onto a silver-coated silicon substrate and aluminum resonators were patterned on top of the graphene using electron beam lithography and liftoff. Figure 4.2a shows an SEM image of the fabricated metamaterial with the FLG flake represented by the shaded area in the image. AFM measurements revealed that the FLG flake was 6 nm thick, which corresponds to 18 layers of graphene, matching the parameters simulated in Figure 4.1c. This layer number was not chosen through design optimization, but was instead chosen because 18 layers is the thinnest FLG flake visible under optical inspection. Admittedly, mechanical exfoliation of FLG provides little control of the spatial arrangement and layer number in each flake and is used here only for fabrication simplicity. In practical devices, large-area FLG flakes with precise layer number could be achieved using multiple CVD graphene transfers.[121, 122]

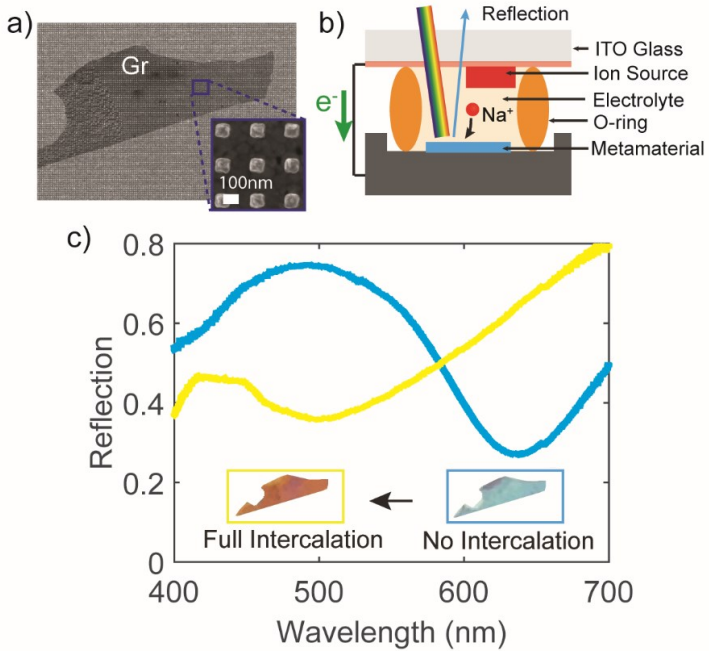

Figure 4.2. Metasurface fabrication and characterization. a) SEM image of fabricated metasurface. Inset shows a closer view of the aluminum resonators. b) Schematic of the electrochemical cell. c) Measured spectral reflectivity for the metasurface in the unintercalated and fully intercalated states.

After fabrication, the metasurface was placed in an electrochemical cell as shown in the Figure 4.2b schematic. The cell uses an $NaPF_6$ electrolyte, an ITO-coated microscope slide for transparent electrical conduction, and a greased o-ring seal to protect the cell from environmental degradation. The reflection spectrum and optical image of the metasurface in the initial, un-intercalated state were captured and displayed in Figure 4.2c. The metasurface appears cyan and the spectral dip nearly matches the simulation prediction in Figure 4.1c. Next, the electrochemical cell is short-circuited allowing sodium ions to fully intercalate the FLG flake. The reflection spectrum was recorded again showing a significant blue-shift in the resonance. The corresponding optical image shows a new metasurface color appearing to be a mixture of yellow and magenta. Because the shape and spectral position of the resonances very nearly match the simulation, we are confident the color change is due to electrochemical actuation of the spacer layer. However, further testing is planned to validate the proposed working mechanism.

4.4 Reversible Color Tuning

To test the reproducibility of the results and reversibility of the color change, another metasurface was fabricated (Figure 4.3a) and loaded into the electrochemical cell. For this test, the cell voltage was modulated between 0V and 2V at 130 msec intervals. Figure 4.3b shows the resulting optical images. The metasurface color oscillates between cyan and yellow, indicating that the response is in fact reversible. Though a 130 msec response time is already faster than previous studies[111, 113], future testing is planned to find the maximum switching speed. Also, future tests will explore the cycle stability and bi-

stability of the device.

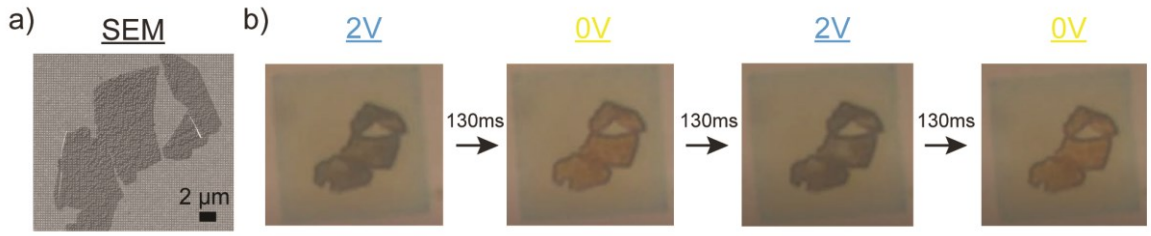

Figure 4.3. Metasurface reversibility testing. a) SEM image of fabricated metasurface. b) Optical images showing the metasurface color at different voltages and time intervals.

4.5 Conclusion

In this work we showed initial results for a metasurface capable of high-speed, reflective color change. We successfully proved that solvent-assisted electrochemical actuation is a viable option for modulating metasurface resonances. Follow-on testing is planned to further characterize the material and measure maximum switching speed, cycle stability, bi-stable hold time, and device power consumption. Though the metasurface was fabricated using non-scalable fabrication processes, future devices could be made with scalable techniques including roll-to-roll nanoimprint lithography and CVD graphene. Beyond reflective visible displays, the electrochemical actuation method presented here could open new opportunities for active metasurfaces in the near to far infrared regions of the spectrum.

Chapter 5: Conclusion

The focus of this research has been to develop practical metamaterial designs with engineered absorption and emission properties. Because these materials derive their optical properties from subwavelength features and not atomic composition, the properties can be precisely tuned for specific applications. In this work, I explored applications including thermophotovoltaic energy conversion, reconfigurable infrared camouflage, and low-power visible displays. However, the results from my work could help solve a broader scope of engineering challenges and help create the next generation of absorbing and emitting materials. In this chapter, I will summarize my results and provide insights into future directions for this research.

5.1 Summary

In Chapter 2, the perfect absorber architecture was used to create a thermal emitter spectrally tuned to emit at the bandgap of a photovoltaic cell. The metamaterial was fabricated over a large area using facile techniques and stable constituent materials. Heating the material to 900 °C for 22 hours showed that the device maintains spectral selectivity in argon-only and argon-oxygen environments. This was the first demonstration of oxygen stability, which is important for thermophotovoltaic emitters as pristine, inert environments have been difficult to achieve in practical devices.[72] The scalable fabrication and stability of this metamaterial design make it a strong candidate for device implementation. However, before manufacturing this material, further testing is needed to

find the maximum device lifetime, as the failure mechanism will most likely be from gold diffusion through the aluminum oxide layers.

In Chapter 3, I demonstrated a metamaterial perfect absorber for thermal emission control that was spatially and temporally modulated with ultraviolet light. Because I used a photomodulation technique, I could achieve spatial control of the emissivity without incorporating electronic pixels. This greatly reduced the complexity of the device for practical implementation. Another interesting aspect of this metamaterial is the use of adsorption and desorption effects in the photoactive layer. These effects increased the photocarrier lifetime, which allowed me to use a low intensity illumination source to achieve the modulation. Low intensity illumination is important for infrared signature control and heat transfer applications, as these applications require emissivity modulation over large areas. Further engineering of the damping loss within the metal components (resonator and backplane) and the carrier dynamics in the spacer layer could further improve both the modulation amplitude and spatial resolution of the emissivity change.

In Chapter 4, I demonstrated a metamaterial perfect absorber architecture for dynamic color generation in the visible spectrum. The large, narrow band absorption provided by the metamaterial gave highly saturated colors in the CMYK subtractive color scheme. Dynamic tuning of the resonant absorption frequency was achieved using solvent-assisted intercalation of a few-layer graphene spacer. The work highlights preliminary results and follow-on testing is planned to assess the full capability of the device. If the material performs as expected, it could revolutionize display technologies for applications including electronic paper and digital signage.

5.2 Outlook

In my opinion, the metamaterial perfect absorber is one of the most promising metamaterial candidates for wide-spread adoption and commercialization. Other metamaterial designs that seek to tailor the reflection and transmission of a material are constantly battling absorption loss that lowers performance efficiency. The perfect absorber design, on the other hand, uses the typically parasitic loss in these resonant structures for a beneficial purpose. This reduces the engineering challenges and material loss requirements associated with the metamaterial design, which should help lower its barrier to marketplace entry.

As mentioned in Chapter 1, the metamaterial architecture has many advantages over conventional absorbers and emitters including spectral, spatial, and polarization control. However, I believe its ability to tune properties post-fabrication is the most important benefit of the design. As demonstrated in Chapters 3 and 4, a dynamic response can provide functionalities not available in natural materials and can help create a new generation of devices. The field of active metamaterial absorbers and emitters is already an aggressively studied topic and should remain so in the near future. Beyond dynamic metamaterials, I believe the field will progress toward solving practical engineering challenges such as integrating the metamaterial architecture with everyday materials.

One opportunity for metamaterial integration could be textile materials for thermal comfort control. The ideal radiative properties of textiles for both cold and hot weather are as follows: In cold weather, the reflectivity should be maximized so that thermal radiation emitted from the body is reflected back to the skin and the energy loss to the environment is reduced[123]. In hot weather, the emissivity or transparency should be maximized to

increase heat dissipation to the environment[124]. It should be noted that these target optical properties are specific to the long-wave infrared part of the spectrum (7-14 μm) where the human body peak emission wavelength occurs. In the visible spectrum, the textile should be opaque and colored to whatever is fashionable. Though previous studies have developed high-reflectivity textiles using silver nanowire coated fabrics[123] and high-transparency textiles using nanoporous polyethylene[125], this area of research is relatively new and remains open to metamaterial absorber architectures.

Another interesting opportunity for integration is building envelopes where the metamaterial can be used to regulate the radiative heat transfer between the building and environment. This technology, termed passive radiative cooling, requires a material with high emissivity at wavelengths corresponding to the transparency window of the atmosphere (7-14μm).[126] That way, the thermal radiation from the building can be rejected to space without absorbing any incoming radiation (space is 3K). Because the cooling requires no power input, this technology has the potential to drastically lower the carbon footprint of both the residential and commercial building sectors. While work has begun to develop metamaterial absorbers for this application,[32] there is still more room for performance improvement.

One of the main challenges for metamaterial absorber/emitter integration is scalable manufacturing. Unlike on-chip photonic devices[127] or biosensors[128] that have small device footprints, most of the applications for this type of metamaterial require large areas (i.e. the surface area of an entire building). Therefore, a major thrust in the field has been to develop techniques that can simply and cheaply fabricate metamaterials over large areas. Some of the more promising techniques include template-based approaches such as anodic

aluminum oxide[129] and nanosphere lithography[130], self-assembly approaches such as dewetting[64] and dip coating,[123] and nanoimprint lithography[131] where the resonator pattern is stamped into a substrate. Whichever fabrication technique proves to be the most efficient and reliable, it must also be compatible with roll-to-roll manufacturing which I believe is the key to metamaterial mass production.

Absorption and emission control with the metamaterial perfect absorber geometry is a stimulating area of research with many future opportunities. Since the metamaterial architecture was proposed nearly ten years ago, the field has shifted from fundamental studies to developing materials with enhanced functionality. In the next ten years, I see a further shift to commercialization, which offers many exciting engineering challenges and opportunities to come.

Appendix A

A.1 Methods

A.1.1 Simulations

Finite-Difference-Time-Domain simulations were performed using the commercial software package, CST Microwave Studio. The parameters of the simulation included a plane wave excitation source at normal incidence, periodic boundary conditions in the x- and y- directions, and perfectly matched layers on top and bottom of the unit cell. ITO ellipsometry data were collected from a 400 nm layer of ITO after annealing the layer at 1173 K for 2 hrs, and the values were fit to a Drude model. The Drude model values (listed in Table A.1) were then used in the simulation. Aluminum oxide was modeled as a lossless dielectric with a permittivity of 3.0. The displayed spectral emissivity is calculated as $\varepsilon=1-\rho$.

A.1.2 Particle Analysis

SEM images of the dewetted gold particles were calibrated in the software program, ImageJ, and the area (A) of each particle was found (Figure A.6). The diameter (D) for each particle was approximated using the following equation: $D = 2\sqrt{\frac{A}{\pi}}$. SEM images from 10 different areas of the sample were taken in order to get a representative distribution of the entire metasurface.

A.1.3 Emissivity Measurements

Room temperature reflection measurements were taken with a Varian Cary 5000 spectrophotometer (0.9-3 μm) and a Bruker Tensor 27 FTIR spectrometer (3-10 μm). Data were collected at an 8° incident angle and calibrated with a gold mirror (Thorlabs). Angle-resolved reflection measurements were performed with a Cary Universal Measurement Accessory (spectrophotometer) and a Seagull Variable Angle Reflection Accessory (FTIR).

A.1.4 Annealing Experiments

The samples were loaded into a Lindberg/Blue M tube furnace and allowed to sit in mTorr-level vacuum for 5 min before the oxygen and argon gases were introduced. For Sample 1, 2.2 sccm of oxygen and 97 sccm of argon were flowed through the tube. For Sample 2, only 100 sccm of argon was added to the tube. A flow valve at the exit of the tube was regulated to maintain the tube pressure near 5 torr. The temperature in the tube was ramped to 1173 K in 1 hour (15 °C min^{-1}) and the annealing timer was started once the tube reached 1173 K. During the cooling period, the temperature set point on the furnace was ramped down at -15 °C min^{-1}, though the temperature in the tube began to significantly lag the set point after 1 hour. The furnace lid was then opened to increase the cooling rate and the sample was allowed to reach ambient temperature (approximately 30 min). After reaching ambient temperature, the tube was vented and the sample removed.

A.2 Supplementary Tables and Figures

Table A.1. ITO Measured Drude Parameters

$\varepsilon_\infty = 4.11$
$\omega_p = 2.64e^{15}$ rad s^{-1}
$\Gamma = 6.41e^{14}$ rad s^{-1}

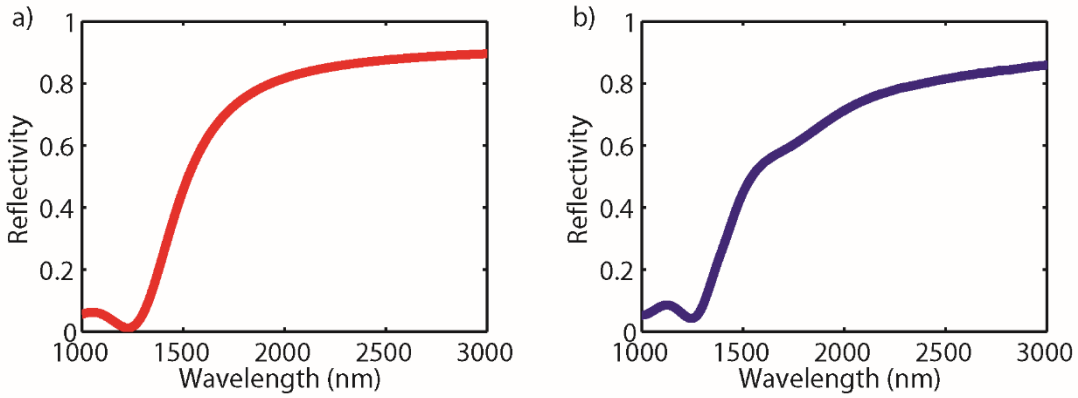

Figure A.1. Spectral reflectivity of 400 nm ITO backplane: (a) simulated and (b) measured. Reflectivity measurements were taken after annealing the ITO for 2 hrs at 1173 K in an argon atmosphere.

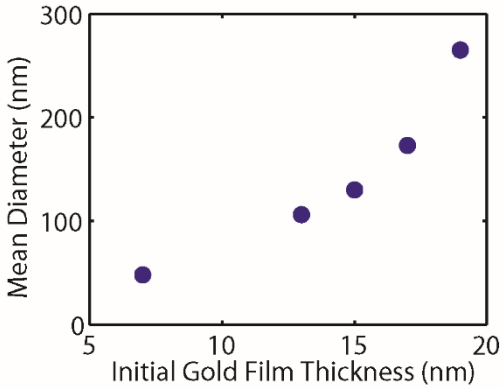

Figure A.2. Mean dewetted gold particle diameter as a function of the initially deposited gold film thickness. The dewetting procedure was kept constant for all samples.

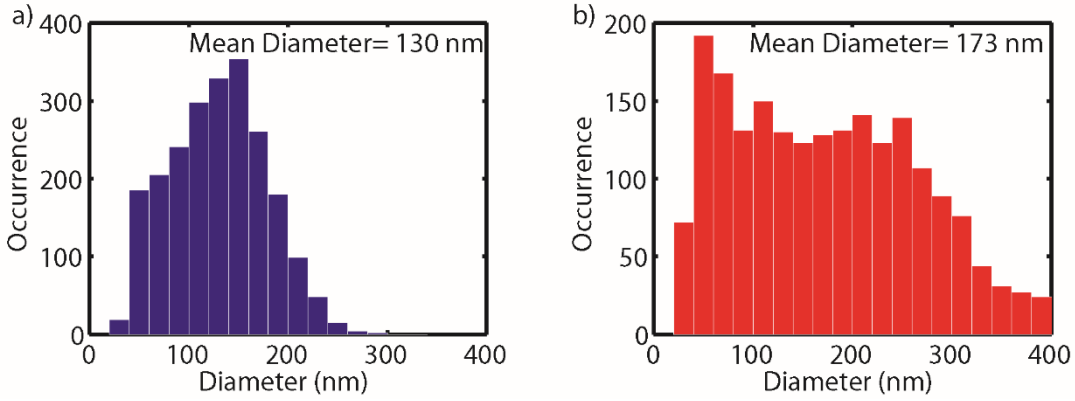

Figure A.3. Particle diameter histogram: (a) Sample 1 and (b) Sample 2. The red-shifted mean diameter of Sample 2 causes the red-shift in peak emissivity of the metamaterial.

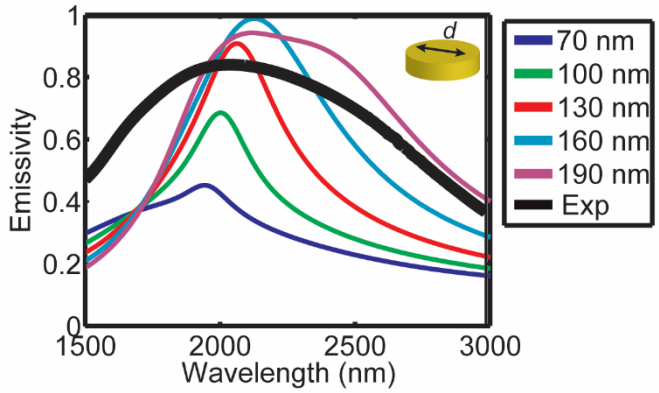

Figure A.4. Simulated emissivity as a function of particle diameter. Simulation parameters were taken from **Figure 2.1** and a particle spacing of 110 nm was maintained throughout the diameter sweep. The black line is the experimentally measured emissivity of Sample 1. The distribution of resonances from the different particle sizes helps create a broad resonance that is centered near the mean particle diameter resonance (130 nm). Deviation from the experimental results is likely due to the ITO optical properties used in the simulation.

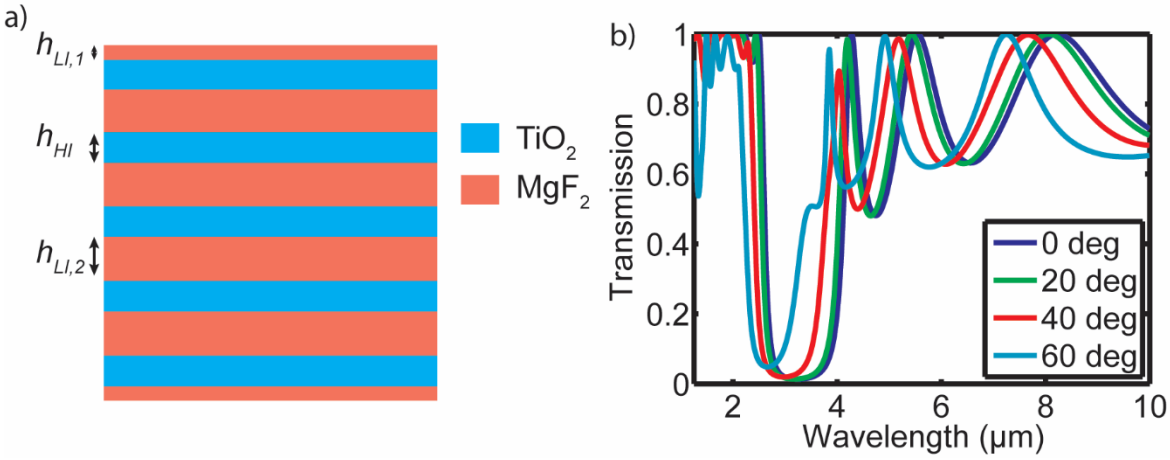

Figure A.5. Cold side filter design. (a) Schematic of simulated filter where $h_{LI,1}$= 287 nm, h_{HI}= 330 nm, and $h_{LI,2}$= 575 nm. (b) Simulated filter transmission averaged over both polarizations and shown as a function of incident angle. All calculations were performed using the normal incidence spectral transmission. The refractive index of TiO_2 was set to 2.39 and the refractive index of MgF_2 was set to 1.37.

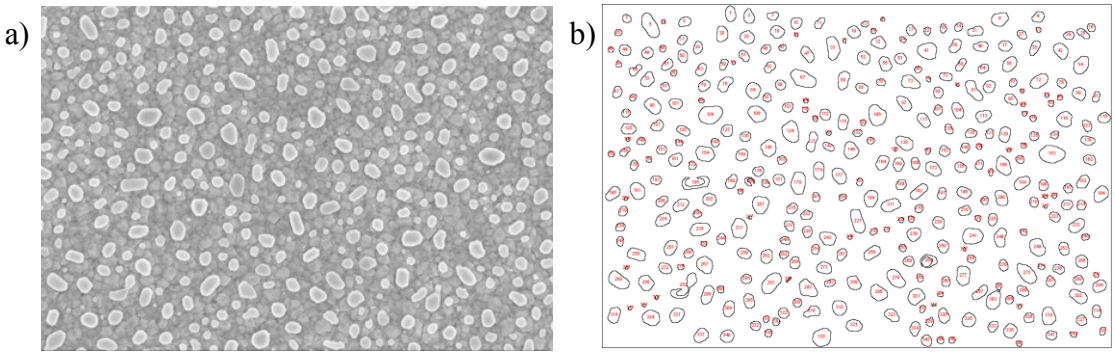

Figure A.6. Particle distribution analysis. (a) SEM image of dewetted gold particles. (b) ImageJ rendering of the particle areas. Particle areas (A) from 10 SEM images taken at different locations on the sample were used to approximate the particle diameters (D) using the following equation: $D = 2\sqrt{\frac{A}{\pi}}$.

Appendix B

B.1 Methods

B.1.1 Simulation

All simulations were performed using the commercial FDTD software package CST Microwave Studio. Each simulation was run with periodic boundary conditions in the x- and y-directions and perfectly matched layers were used along the propagation directions. The simulations were constructed using the dimensions and material properties listed in Appendix B.2.

B.1.2 Fabrication

All ITO films were sputtered at 350 °C in a 2 mTorr atmosphere with O_2 (0.2 sccm) and Ar (20 sccm). The n-ZnO film was sputtered at 200 °C in a 10 mTorr atmosphere with O_2 (0.2 sccm) and Ar (20 sccm). The a-ZnO film was deposited with the same conditions, except the substrate was not heated. The resonators were created with photolithography and electron beam deposition of 5 nm titanium and 70 nm gold.

B.1.3 Characterization

The infrared spectral reflectivity of the films was measured in a FTIR spectrometer using a variable angle attachment set to 10° and a gold mirror as reference. The emissivity

modulation was characterized using the same FTIR setup, except UV light was directed onto the sample. The UV source was an LED flashlight (Intsun SK66) with a center wavelength of 365 nm. The sample was illuminated for one minute before the infrared spectrum was taken to ensure steady-state; the sample was illuminated during the measurement. The UV light was blocked from the detector using a wire grid polarizer with KRS-5 substrate. The reported UV intensities were found by measuring the illumination power and dividing by the illumination area on the sample. Therefore, the listed intensities describe the intensity at the material surface.

For the thermal camera measurements, the camera emissivity and refresh rate were set to 0.95 and 25 Hz, respectively. The camera has an accuracy of ±2 °C. For the front-side illumination, the camera angle was roughly 20° from normal while the camera angle for back-side illumination was at normal incidence. The numerical aperture of the focusing lens was NA=0.13. The focused beam diameter on the sample was approximately 4 mm. The temperature of the hotplate was measured with a type-K thermocouple that has an accuracy of ±2.2 °C. A ring-shaped thermoelectric heater was used for the back-side illumination measurements to allow transmission of UV light. Back-side illumination measurements were also taken with the a-ZnO film to ensure the UV light was not causing the camera to give a false thermal image (Figure B.8).

B.2 Metamaterial Simulation Parameters and Design Optimization

Figure B.1a shows the metamaterial unit cell including the simulated dimensions. In Figure B.1b, the n-ZnO spacer height is increased from 550 nm to 1150 nm which causes a decrease in the peak emissivity at the resonant wavelength. This is a result of

decreased coupling between the gold resonator and the ITO backplane, which causes an increase in Γ_r for the metamaterial. To determine the appropriate spacer height, the percent emissivity modulation at each spacer height was calculated using simulations where the ZnO carrier concentration, n_{ZnO}, was modulated from $n_{ZnO,1}$=3e17 cm^{-3} to $n_{ZnO,2}$=7e17 cm^{-3}. These carrier concentrations, which were estimated from measured dark and UV illuminated spectral emissivities, change the ZnO optical properties as shown in Figure B.1c and Figure B.1d. The figure of merit (*FOM*) for each spacer height is displayed in Figure B.1e and shows a peak at 950 nm. The *FOM* was calculated using the following equations:

$$E_{MM}(\lambda, T, n_{ZnO}) = \int_{\lambda_{low}=7.5\mu m}^{\lambda_{high}=14\mu m} \varepsilon(\lambda, n_{ZnO}) \frac{2\pi h {c_o}^2}{\lambda^5 \left[exp\left(\frac{hc_o}{\lambda k_B T}\right) - 1\right]} d\lambda \tag{B.1}$$

$$E_{BB}(\lambda, T) = \int_{\lambda_{low}=7.5\mu m}^{\lambda_{high}=14\mu m} \frac{2\pi h {c_o}^2}{\lambda^5 \left[exp\left(\frac{hc_o}{\lambda k_B T}\right) - 1\right]} d\lambda \tag{B.2}$$

$$FOM = \frac{\Delta\varepsilon}{\varepsilon_o} = \frac{\left(\frac{E_{MM,n_{ZnO,2}}}{E_{BB}}\right) - \left(\frac{E_{MM,n_{ZnO,1}}}{E_{BB}}\right)}{\left(\frac{E_{MM,n_{ZnO,1}}}{E_{BB}}\right)} \tag{B.3}$$

where λ_{high} and λ_{low} are the spectral limits of the thermal camera, ε is the simulated emissivity, h is the Planck constant, c_o is the speed of light in vacuum, k_b is Boltzmann's constant, and T is 423 K. Figure B.1f shows the modulated spectral emissivity for a spacer height of 950 nm. The modulated spectral emissivity shows good agreement with the measured values in the main text.

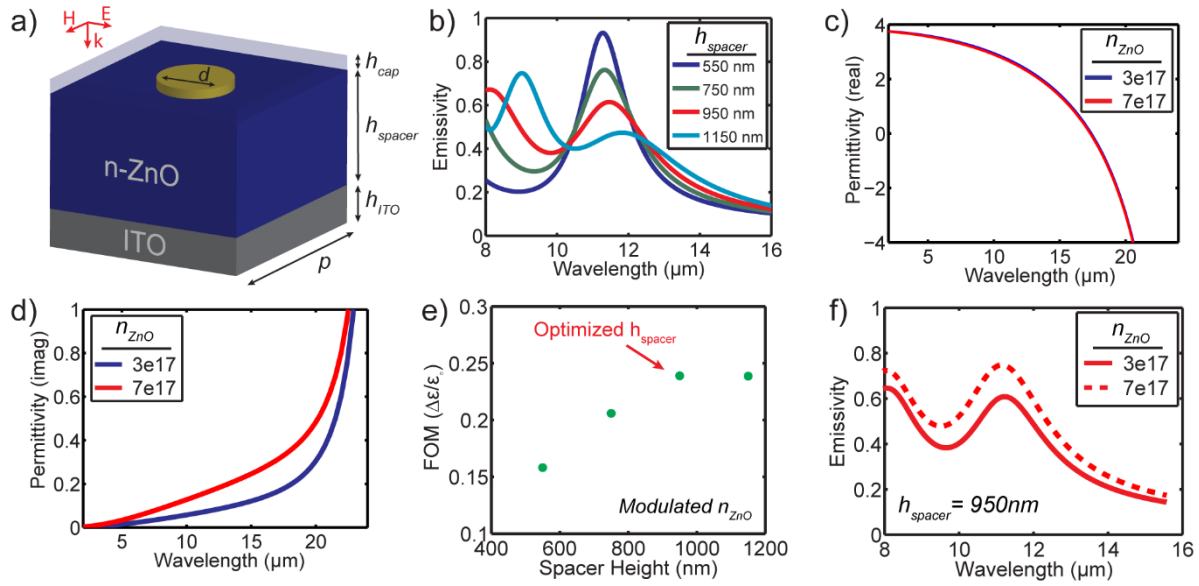

Figure B.1. Simulated metamaterial. a) Unit cell where d=2900 nm, h_{cap}=40 nm, h_{ITO}=400 nm, and p=6000 nm. b) Simulated emissivity with variable n-ZnO spacer height (h_{spacer}). c,d) Change in the real(c) and imaginary(d) parts of the ZnO permittivity when the carrier concentration is increased from 3e17 to 7e17 cm^{-3}. e) Percent change of emissivity (*FOM*) at various spacer heights when n_{ZnO} is modulated between 3e17 and 7e17 cm^{-3}. The optimized spacer height is 950 nm. d) Simulated emissivity modulation for spacer height of 950 nm.

Table B.1. Simulation Optical Properties

ZnO parameters [1]	ITO Parameters[a)]	Au Parameters
$\varepsilon_{\infty,ZnO} = 3$	$\varepsilon_{\infty,ITO} = 4$	Properties from [2]
$\omega_{LO,ZnO} = 1.09e1$ rad s^{-1}	$\omega_{p,ITO} = 1.84e1$ rad s^{-1}	
$\omega_{TO,ZnO} = 7.23e1$ rad s^{-1}	$\Gamma_{ITO} = 4.1e1$ rad s^{-1}	
$\gamma_{ZnO} = 1e1$ rad s^{-1}		
$\Gamma_{ZnO} = 3e1$ rad s^{-1}		

[a)] Properties fit from experimental data

B.3 Integrated Emissivity Calculation

We compared our work to previous low-power, ultra-thin emissivity modulators

with calculations of the integrated emissivity change. Integrated emissivity change is important for radiative heat transfer and infrared signature control applications which rely on total emitted flux to control cooling power and apparent temperature change, respectively. The integrated emissivities (ε_{int}) were found by first using Equation (B.1) and (B.2) to calculate E_{MM} and E_{BB}. Then ε_{int} was simply calculated from, $\varepsilon_{int} = E_{MM}/E_{BB}$. The difference between the initial integrated emissivity and modulated integrated emissivity is $\Delta\varepsilon_{int}$.

The spectral emissive power for this work and the previous studies are plotted in Figure B.2. The data for the previous studies were extracted from published work. The integrated emissivity change for this work is $\Delta\varepsilon_{int}\approx0.12$, and the integrated emissivity changes for ref [3] and ref [4] are $\Delta\varepsilon_{int}\approx0.02$ and $\Delta\varepsilon_{int}\approx0.002$, respectively. The lower limit of integration for ref [4] was extended to 6.5 μm to include the emissivity modulation in this spectral region.

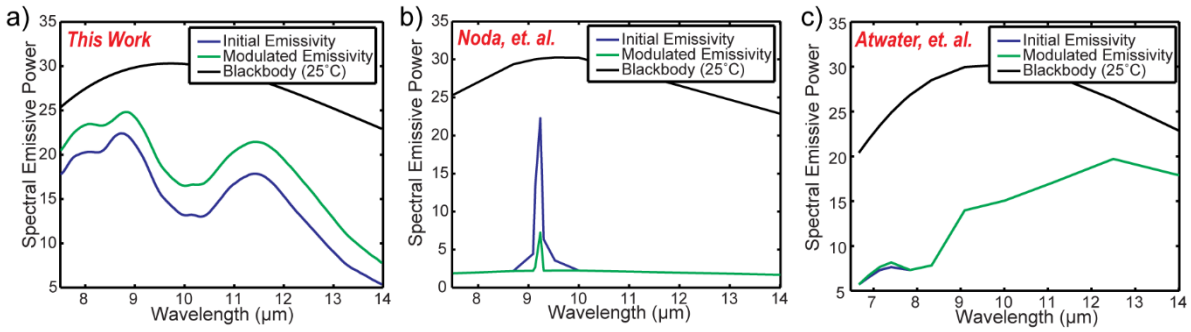

Figure B.2. Spectral emissive power for low-power, ultra-thin emissivity modulators. a) Results from this work. b) Data from Ref [3]. c) Data from Ref [4].

B.4 Anti-Reflection Absorber Analysis

Figure B.3a shows the simulated emissivity for the dark and UV-illuminated anti-reflection films using the same estimated carrier concentrations of Appendix B.2 (3e17 and 7e17 cm^{-3}). The simulated peak change in emissivity ($\Delta\varepsilon \approx 0.055$) is similar to the measured response in Figure 3.2c of the main text ($\Delta\varepsilon \approx 0.045$). The film in the main text is then annealed in a tube furnace at 350 °C with 100 sccm H_2 for 1 hr. Annealing with hydrogen has been shown to passivate ZnO nanocrystallite surfaces and reduce the adsorption of oxygen.[98, 99] This passivated film should possess a higher initial free carrier concentration because less electrons are trapped at the nanocrystal interfaces, and the modulation of free carrier concentration should be reduced because of the decreased hole trapping capability. Both of these effects are seen in the experimentally measured film (Figure B.3b, red curves). After hydrogen annealing, the dark emissivity increases due to the increased carrier concentration and the modulated emissivity ($\Delta\varepsilon \approx 0.015$) is reduced to roughly one-third of the as-deposited film. The film was then annealed in air at 250 °C for 1 hr to depassivate the film. As seen in Figure B.3b (blue curves), the original dark emissivity and modulated emissivity are mostly recovered.

Figure B.3c and Figure B.3d show electric field plots for a unit cell of the (c) metamaterial and (d) anti-reflection film. Both plots are shown with the same scale which allows for direct comparison of the electric field concentration. It is evident from the figures that the metamaterial provides a much larger field concentration in the n-ZnO spacer layer when compared to the anti-reflection absorber. Because the metamaterial provides higher electric-field mode confinement within the active layer, similar changes in carrier concentration will result in larger changes in emissivity as was demonstrated in the

main text.

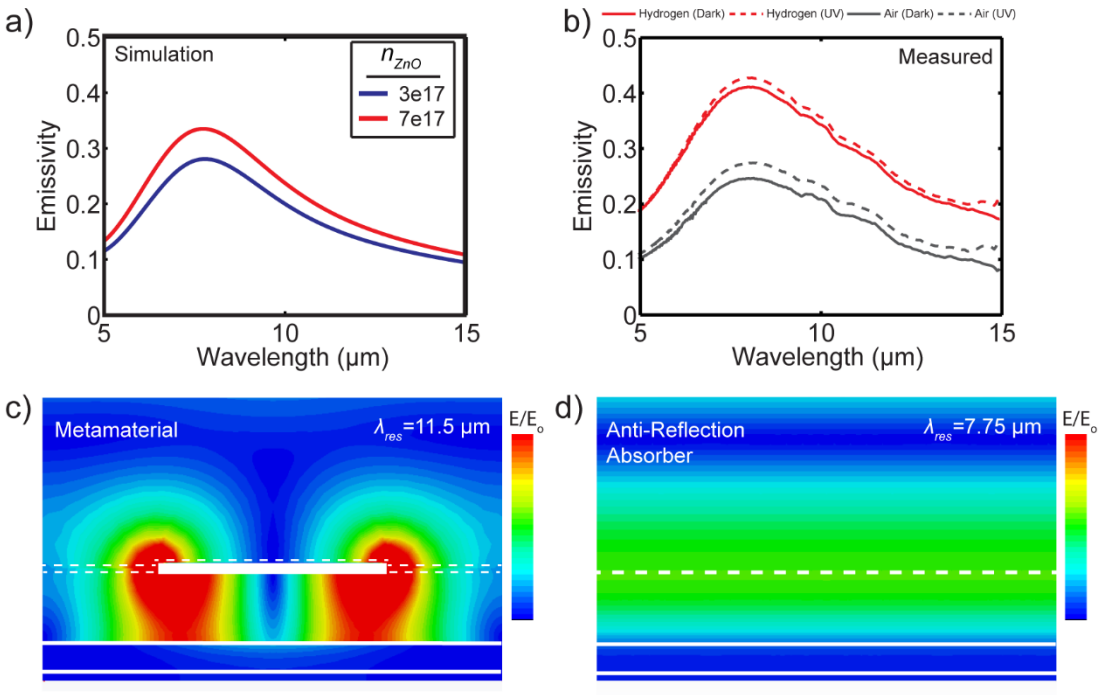

Figure B.3. Anti-reflection absorber simulations and experimental demonstrations. a) Simulated emissivity with variable n-ZnO carrier concentration. b) Measured emissivity after annealing in different atmospheres. Solid lines indicate the dark emissivity and dashed lines represent the measured emissivity during UV illumination. c,d) Plots of the absolute value of the electric field for the c) metamaterial unit cell and d) anti-reflection absorber unit cell. Cross-sections were taken through the middle of each unit cell at the resonant frequency (λ_{res}) of each material. Both c) and d) are plotted with the same electric field scale.

B.5 Calculation of Photoinduced Heating from Ultraviolet Illumination

Figure B.4a shows the measured absorption spectrum of the metamaterial and a-ZnO film. At the spectral position of the illumination source, 365 nm, both samples have virtually the same absorption and therefore any photoheating effects will be experienced equally for both samples. Results in the main text show that the a-ZnO film experiences no

apparent temperature rise upon UV illumination, which suggests that photoheating is negligible. To confirm this result, a thermal model of the sample was constructed in COMSOL. Because the model is being used to ensure the sample doesn't heat too much during the UV illumination, we use conservative boundary conditions to get an upper bound of the temperature rise. That way, if the calculated temperature rise is negligibly small, we can safely assume that the actual temperature rise is negligibly small.

Figure B.4b shows a schematic of the thermal model which includes a circular surface heat flux to represent the UV illumination input and a fully insulated sapphire substrate at all other boundaries. The insulated substrate provides an extremely conservative boundary condition since, in the actual sample, heat will be dissipated by conduction, convection, and radiation through the substrate surfaces. The parameters listed in Table B.2 were input to the simulation and the transient model was calculated out to t=20 sec to match the experimental condition. The results of the simulation, Figure B.4c, show a maximum temperature rise of ΔT=0.10 °C. Because this upper bound of the temperature rise is negligibly small, we can confidently conclude that photoheating in the metamaterial is negligible.

Table B.2. Simulation Parameters

Parameter	Value
Thickness (*h*)	0.5 mm
Sample Length (*L*)	18 mm
Sample Width (*w*)	13 mm
Spot Diameter (*D*)	4 mm
Spot x-loc (*x*)	4 mm
Spot y-loc (*y*)	2 mm
Density (ρ)	3980 kgm^{-3}
Thermal Conductivity (*k*)	25 $Wm^{-1}K^{-1}$
Specific Heat (C_p)	756 $Jkg^{-1}K^{-1}$
Spot Heating (*q''*)	100 Wm^{-2}

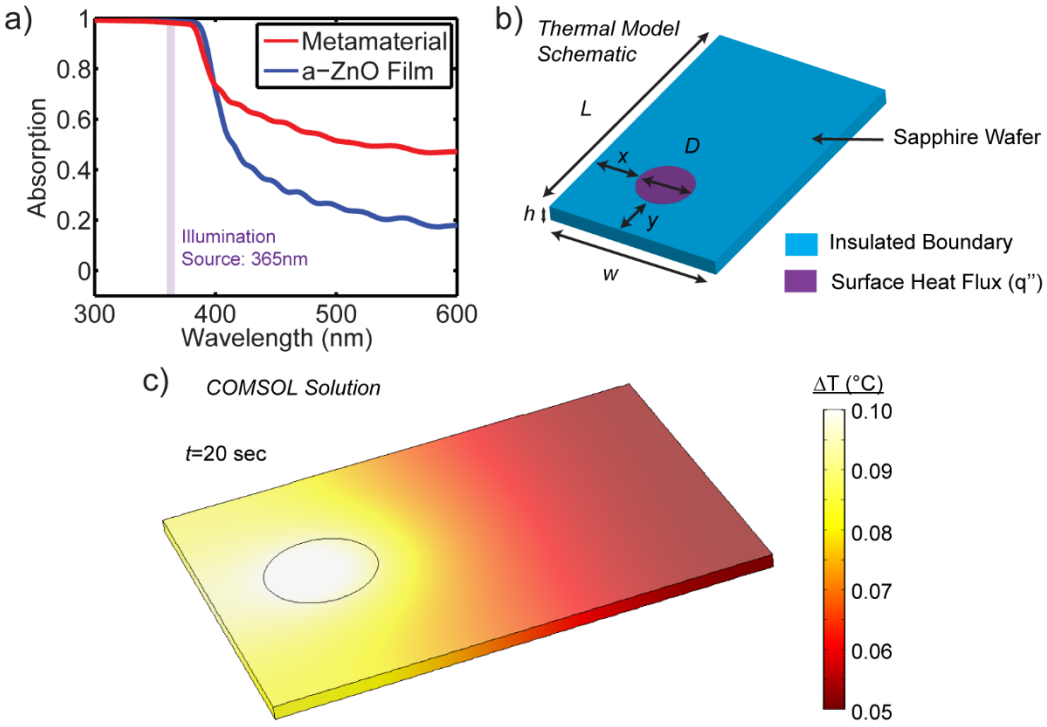

Figure B.4. UV photoinduced heating. a) Measured UV absorption spectrum of metamaterial and a-ZnO film. b) Thermal model schematic of metamaterial film with UV illumination. All boundaries outside of the surface heat flux boundary are assumed to be insulated. c) Results from COMSOL simulation at *t*=20 sec.

The COMSOL simulation was verified using an analytical solution for a two-dimensional axisymmetric cylinder of height h where the UV heating occurs at the centerline (r=0) on the top surface (z=0). The top and bottom surfaces are insulated and the cylinder is assumed to be radially infinite. The maximum temperature rise occurs at the centerline of the top surface, $\theta_{max}(t) = \theta(0,0,t)$, which can be calculated using the following expression:

$$\theta(0,0,t) = 2Q\sqrt{Fo}\left\{\frac{1}{\sqrt{\pi}} - ierfc\left(\frac{1}{2\sqrt{Fo}}\right) + 2\sum_{m=1}^{\infty}\left[ierfc\left(\frac{mh^*}{\sqrt{Fo}}\right) - ierfc\left(\sqrt{\frac{1}{4Fo} + \frac{m^2h^{*2}}{Fo}}\right)\right]\right\} \quad \text{(B.4)}$$

In the foregoing expression, $R=D/2$, $Q=q''R/k$, $Fo=\alpha t/R^2$, $h^*=h/R$, and the thermal diffusivity is $\alpha=k/\rho C_p$. The ierfc is the integral error function written as $\text{ierfc}(x)=-x\text{erfc}(x)+\exp(-x^2)/\sqrt{\pi}$. At a time of t=20 sec, the analytical solution provides a maximum temperature rise of 0.045 °C. Modifying the previous COMSOL simulation to match the boundary conditions of the analytical solution requires L and w to be made at least as large as the thermal penetration depth, $L = \sqrt{\alpha t}$, so that the radial boundary has no effect on the solution and the infinite boundary assumption is valid. When the L and w dimensions are increased to 50 mm, the temperature rise at the UV spot heating is 0.045 °C as shown in Figure B.5. Because this solution matches the analytical solution, we can be sure that the COMSOL model was properly implemented and the results shown in Figure B.4c are valid.

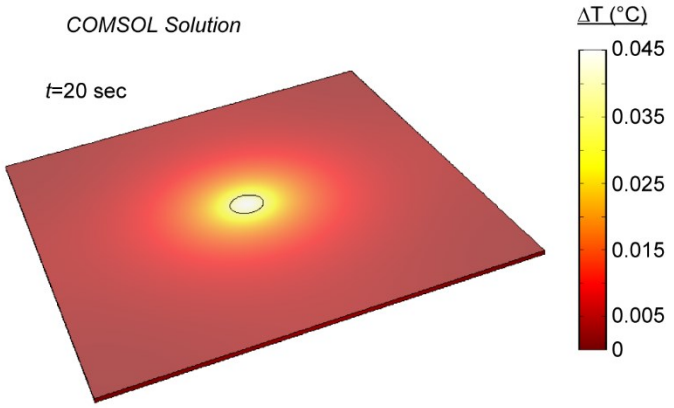

Figure B.5. COMSOL simulation result using boundary conditions matching the analytical model.

B.6 Multi-excitation Plot for Metamaterial Temporal Response

The experiment from Figure 3.3 in the main text was repeated to investigate the effects of multiple UV excitations. In this experiment, the temperature of the substrate was 150 °C and the UV intensity at the metamaterial surface was 6 mW/cm^{-2}. The results from the study, Figure B.6, show that the emissivity decays to zero each time which indicates that no fatigue-like behavior is present in the material.

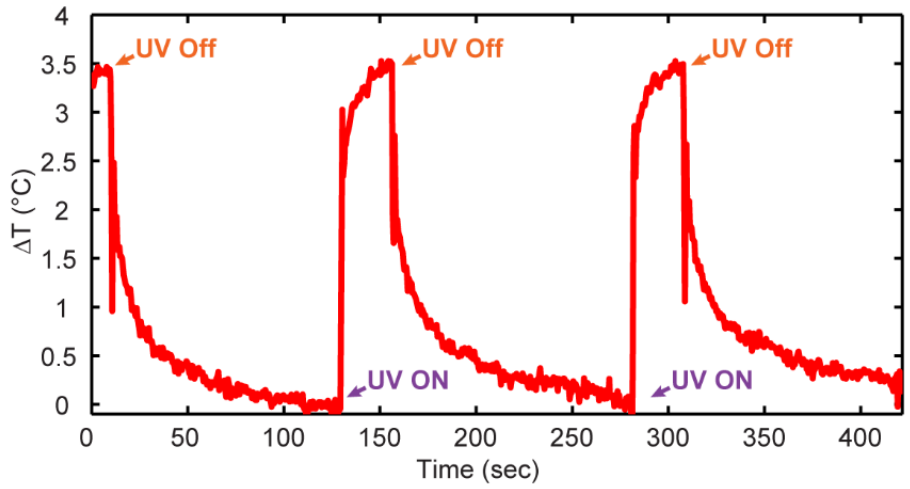

Figure B.6. Multi-excitation temporal plot of the metamaterial. The arrows indicate when the UV source was turned off, "UV Off", and when the UV source was turned on, "UV ON".

B.7 Spatial Contrast Measurement

The spatial resolution of the metamaterial emissivity modulator was characterized by projecting an image of a Ronchi ruling onto the metamaterial. A Ronchi ruling (Figure B.7a) possesses equal bar and space patterns and is a standard test target used to measure optical contrast. The thermal image of the illuminated metamaterial is shown in Figure B.7a which also includes a magnified region of the sample. Figure B.7b shows an x-direction slice across the magnified region of the sample with normalized ΔT plotted as a function of position. The temperature rise was normalized for easier visualization of the contrast. The plot resolution in Figure B.7b is degraded due to low pixel resolution of the camera; however, we can still extract estimated values of the bar spacing and optical contrast.

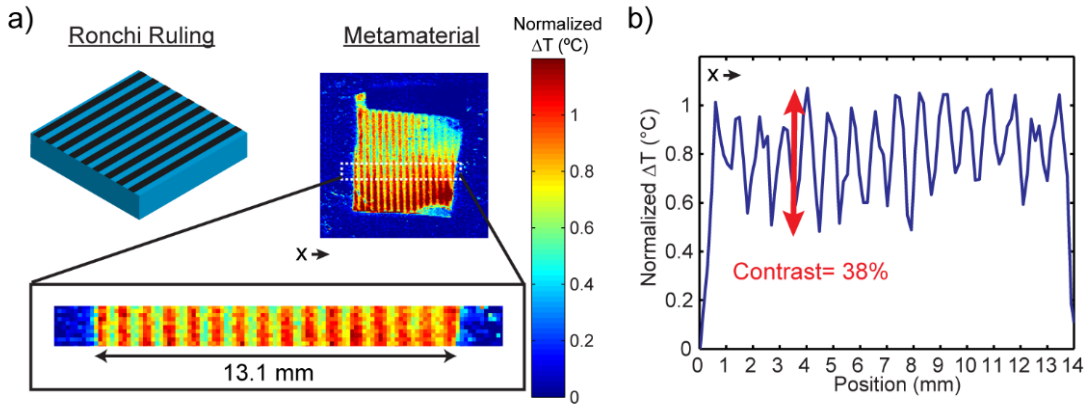

Figure B.7. Spatial contrast measurement of the metamaterial. a) Schematic of the Ronchi ruling, which was used as a projection mask during the metamaterial illumination, and thermal image of the metamaterial showing the normalized temperature rise ΔT. A magnified image was included for further clarity. b) X-direction slice of the normalized ΔT taken across the magnified region of a).

Measuring the peak-to-peak distances in the plot, we find that the period of the ruling is approximately 900 μm. This means that each projected linewidth is approximately 450 μm. Using Equation (B.5) we find largest contrast to be 38%. Because of the poor pixel resolution of the thermal camera we can't resolve the full maximum and minimum temperature change of each line-pair. This means calculating an average contrast of neighboring line-pairs will provide an artificially low contrast value. Therefore, we report only the maximum contrast value, 38%, in the main text.

$$\%\ Contrast = \left[\frac{(\Delta T_{max} - \Delta T_{min})}{(\Delta T_{max} + \Delta T_{min})}\right] \times 100 \tag{B.5}$$

B.8 Back-side Illumination with a-ZnO

The a-ZnO anti-reflection film was tested using the same back-side illumination conditions as the metamaterial in the main text, and the resulting thermal signature is displayed in Figure B.8. As expected, no discernable temperature change is detected. This indicates that the thermal images captured in the main text were indeed from an emissivity change in the metamaterial and not from transmission of the UV source.

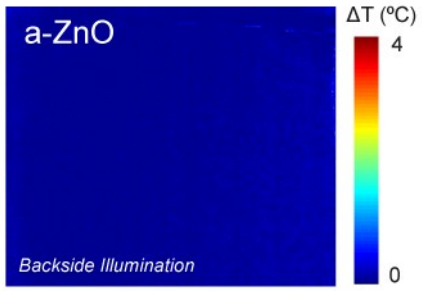

Figure B.8. Thermal image of a-ZnO anti-reflection film during back-side illumination with the grayscale UV mask.

BIBLIOGRAPHY

[1] R. Walser, in *Proceedings of SPIE*, **2001**, 1.

[2] D. Schurig, J. J. Mock, B. J. Justice, S. A. Cummer, J. B. Pendry, A. F. Starr, and D. R. Smith, *Science* **2006**, *314*, 977.

[3] R. Liu, C. Ji, J. J. Mock, J. Y. Chin, and T. J. Cui, *Science* **2009**, *323*, 366.

[4] J. Valentine, J. Li, T. Zentgraf, G. Bartal, and X. Zhang, *Nat. Mater.* **2009**, *8*, 568.

[5] T. Ergin, N. Stenger, P. Brenner, J. B. Pendry, and M. Wegener, *Science* **2010**, *328*, 337.

[6] D. R. Smith, J. B. Pendry, and M. C. K. Wiltshire, *Science* **2004**, *305*, 788.

[7] J. Valentine, S. Zhang, T. Zentgraf, E. Ulin-Avila, D. A. Genov, G. Bartal, and X. Zhang, *Nature* **2008**, *455*, 376.

[8] R. Shelby, D. R. Smith, and S. Schultz, *Science* **2001**, *292*, 77.

[9] P. Moitra, Y. Yang, Z. Anderson, I. I. Kravchenko, D. P. Briggs, and J. Valentine, *Nat. Photonics* **2013**, *7*, 791.

[10] R. Maas, J. Parsons, N. Engheta, and A. Polman, *Nat. Photonics* **2013**, *7*, 907.

[11] N. Yu and F. Capasso, *Nat. Mater.* **2014**, *13*, 139.

[12] F. Aieta, M. A. Kats, P. Genevet, and F. Capasso, *Science* **2015**, *2*, 1342.

[13] Q. Wang, E. T. F. Rogers, B. Gholipour, C.-M. Wang, G. Yuan, J. Teng, and N. I. Zheludev, *Nat. Photonics* **2015**, *10*, 60.

[14] W. Lewandowski, M. Fruhnert, J. Mieczkowski, C. Rockstuhl, and E. Górecka, *Nat. Commun.* **2015**, *6*, 6590.

[15] M. Fox, *Optical Properties of Solids*, OUP Oxford, Oxford, **2010**.

[16] R. P. Feynman, R. B. Leighton, and M. Sands, *The Feynman lectures on physics*, Addison-Wesley Pub. Co., Reading, **1965**.

[17] J. A. Schuller, E. S. Barnard, W. Cai, Y. C. Jun, J. S. White, and M. L. Brongersma, *Nat. Mater.* **2010**, *9*, 193.

[18] J. R. Adleman, D. A. Boyd, D. G. Goodwin, and D. Psaltis, *Nano Lett.* **2009**, *9*, 4417.

[19] W. A. Challener, C. Peng, A. V. Itagi, D. Karns, W. Peng, Y. Peng, X. Yang, X. Zhu, N. J. Gokemeijer, Y.-T. Hsia, G. Ju, R. E. Rottmayer, M. A. Seigler, and E. C. Gage, *Nat. Photonics* **2009**, *3*, 220.

[20] L. Wang and B. Li, *Phys. Rev. Lett.* **2008**, *101*, 1.

[21] C. Loo, A. Lowery, N. Halas, J. West, and R. Drezek, *Nano Lett.* **2005**, *5*, 709.

[22] Z. J. Coppens, W. Li, D. G. Walker, and J. G. Valentine, *Nano Lett.* **2013**, *13*, 1023.

[23] N. Landy, S. Sajuyigbe, J. Mock, D. Smith, and W. Padilla, *Phys. Rev. Lett.* **2008**, *100*, 207402.

[24] T. A. I. Noue, M. E. D. E. Z. Oysa, T. A. A. Sano, and S. U. N. Oda, **2015**, *2*, 27.

[25] J. Hao, J. Wang, X. Liu, W. J. Padilla, L. Zhou, and M. Qiu, *Appl. Phys. Lett.* **2010**, *96*, 251104.

[26] X. Liu, T. Starr, A. F. Starr, and W. J. Padilla, *Phys. Rev. Lett.* **2010**, *104*, 207403.

[27] W. Li, U. Guler, N. Kinsey, G. V Naik, A. Boltasseva, J. Guan, V. M. Shalaev, and A. V Kildishev, *Adv. Mater.* **2014**, *26*, 1.

[28] C. Wu, B. Neuner III, J. John, A. Milder, B. Zollars, S. Savoy, and G. Shvets, *J. Opt.* **2012**, *14*, 24005.

[29] G. M. Akselrod, J. Huang, T. B. Hoang, P. T. Bowen, L. Su, D. R. Smith, and M. H. Mikkelsen, *Adv. Mater.* **2015**, n/a.

[30] T. Cao, C.-W. Wei, R. E. Simpson, L. Zhang, and M. J. Cryan, *Sci. Rep.* **2014**, *4*, 3955.

[31] Z. Zhu, P. G. Evans, R. F. Haglund, and J. G. Valentine, *Nano Lett.* **2017**, *17*, 4881.

[32] M. M. Hossain, B. Jia, and M. Gu, *Adv. Opt. Mater.* **2015**, *3*, 1047.

[33] X. Liu, T. Tyler, T. Starr, A. F. Starr, N. M. Jokerst, and W. J. Padilla, *Phys. Rev. Lett.* **2011**, *107*, 45901.

[34] X. Liu and W. J. Padilla, *Adv. Mater.* **2016**, *28*, 871.

[35] Z. J. Coppens, I. I. Kravchenko, and J. G. Valentine, *Adv. Opt. Mater.* **2016**, *4*, 671.

[36] C. Shemelya, D. DeMeo, N. P. Latham, X. Wu, C. Bingham, W. Padilla, and T. E. Vandervelde, *Appl. Phys. Lett.* **2014**, *104*, 201113.

[37] D. Woolf, J. Hensley, J. G. Cederberg, D. T. Bethke, A. D. Grine, and E. A. Shaner, *Appl. Phys. Lett.* **2014**, *105*, 81110.

[38] J. A. Mason, S. Smith, and D. Wasserman, *Appl. Phys. Lett.* **2011**, *98*, 2009.

[39] A. Tittl, A. K. U. Michel, M. Schaferling, X. Yin, B. Gholipour, L. Cui, M. Wuttig, T. Taubner, F. Neubrech, and H. Giessen, *Adv. Mater.* **2015**, *27*, 4597.

[40] M. Makhsiyan, P. Bouchon, J. Jaeck, J. L. Pelouard, and R. Haïdar, *Appl. Phys. Lett.* **2015**, *107*, 20.

[41] T. Bauer, *Thermophotovoltaics: Basic Principles and Critical Aspects of System Design*, Springer, Berlin, **2011**.

[42] W. R. Chan, P. Bermel, R. C. N. Pilawa-Podgurski, C. H. Marton, K. F. Jensen, J. J. Senkevich, J. D. Joannopoulos, M. Soljacic, and I. Celanovic, *Proc. Natl. Acad. Sci. U. S. A.* **2013**, *110*, 5309.

[43] T. Coutts and M. Fitzgerald, *Phys. World* **1998**, *11*, 49.

[44] L. Fraas, J. Avery, E. Malfa, J. G. Wuenning, G. Kovacio, and C. Astle, *AIP Conf.*

Proc. **2003**, *61*, 653.

[45] C. L. DeBellis, M. V Scotto, L. Fraas, J. Samaras, R. C. Watson, and S. W. Scoles, *AIP Conf. Proc.* **1999**, *460*, 70.

[46] N. Harder and P. Wurfel, *Semicond. Sci. Technol.* **2003**, *18*, S151.

[47] I. E. Khodasevych, L. Wang, A. Mitchell, and G. Rosengarten, *Adv. Opt. Mater.* **2015**, *3*, 852.

[48] A. Lenert, D. M. Bierman, Y. Nam, W. R. Chan, I. Celanović, M. Soljačić, and E. N. Wang, *Nat. Nanotechnol.* **2014**, *9*, 126.

[49] V. Rinnerbauer, A. Lenert, D. M. Bierman, Y. X. Yeng, W. R. Chan, R. D. Geil, J. J. Senkevich, J. D. Joannopoulos, E. N. Wang, M. Soljačić, and I. Celanovic, *Adv. Energy Mater.* **2014**, *4*, 1.

[50] J. B. Chou, Y. X. Yeng, Y. E. Lee, A. Lenert, V. Rinnerbauer, I. Celanovic, M. Soljačić, N. X. Fang, E. N. Wang, and S.-G. Kim, *Adv. Mater.* **2014**, *26*, 8041.

[51] K. A. Arpin, M. D. Losego, A. N. Cloud, H. Ning, J. Mallek, N. P. Sergeant, L. Zhu, Z. Yu, B. Kalanyan, G. N. Parsons, G. S. Girolami, J. R. Abelson, S. Fan, and P. Braun, *Nat. Commun.* **2013**, *4*, 2630.

[52] Y. X. Yeng, M. Ghebrebrhan, P. Bermel, W. R. Chan, J. D. Joannopoulos, M. Soljačić, and I. Celanovic, *Proc. Natl. Acad. Sci. U. S. A.* **2012**, *109*, 2280.

[53] U. Guler, A. Boltasseva, and V. M. Shalaev, *Science* **2014**, *344*, 263.

[54] P. B. Johnson and R. W. Christy, *Phys. Rev. B* **1972**, *6*, 10.

[55] C. A. Wang, H. K. Choi, S. L. Ransom, G. W. Charache, L. R. Danielson, and D. M. DePoy, *Appl. Phys. Lett.* **1999**, *75*, 1305.

[56] P. R. West, S. Ishii, G. V. Naik, N. K. Emani, V. M. Shalaev, and A. Boltasseva, *Laser Photon. Rev.* **2010**, *4*, 795.

[57] J. Park, J.-H. Kang, X. Liu, and M. L. Brongersma, *Sci. Rep.* **2015**, *5*, 15754.

[58] D. B. Tice, S. Q. Li, M. Tagliazucchi, D. B. Buchholz, E. A. Weiss, and R. P. H. Chang, *Nano Lett.* **2014**, *14*, 1120.

[59] O. J. Gregory, Q. Luo, and E. E. Crisman, *Thin Solid Films* **2002**, *406*, 286.

[60] O. J. Gregory and Q. Luo, *Sensors Actuators, A Phys.* **2001**, *88*, 234.

[61] S. E. Dyer, O. J. Gregory, P. S. Amons, and A. B. Slot, *Thin Solid Films* **1996**, *288*, 279.

[62] N. Karker, G. Dharmalingam, and M. A. Carpenter, *ACS Nano* **2014**, *8*, 43.

[63] N. A. Joy, B. K. Janiszewski, S. Novak, T. W. Johnson, S. Oh, A. Raghunathan, J. Hartley, and M. A. Carpenter, *J. Phys. Chem. C* **2013**, *117*, 11718.

[64] A. B. Tesler, L. Chuntonov, T. Karakouz, T. Bendikov, G. Haran, A. Vaskevich, and I. Rubinstein, *J. Phys. Chem. C* **2011**, *115*, 24642.

[65] P. Farzinpour, A. Sundar, K. D. Gilroy, Z. E. Eskin, R. Hughes, and S. Neretina,

Nanotechnology **2012**, *23*, 495604.

[66] Z. Liu, X. Liu, S. Huang, P. Pan, J. Chen, G. Liu, and G. Gu, *ACS Appl. Mater. Interfaces* **2015**, *7*, 4962.

[67] H. G. Riveros, *Phys. Educ.* **2006**, *41*, 1.

[68] D. L. Chubb, *Fundamentals of Thermophotovoltaic Energy Conversion*, Elsevier B.V., Amsterdam, **2007**.

[69] W. Shockley and H. J. Queisser, *J. Appl. Phys.* **1961**, *32*, 510.

[70] G. Frank and H. Kostlin, *Appl. Phys. A* **1982**, *27*, 197.

[71] N. Yamada, I. Yasui, Y. Shigesato, H. Li, Y. Ujihira, and K. Nomura, *Jpn. J. Appl. Phys.* **2000**, *39*, 4158.

[72] E. Doyle, K. Shukla, and C. Metcalfe, *Natl. Aeronaut. Sp. Adm. Tech. Rep. TR04-2001* **2001**, 1.

[73] S. L. Firebaugh, K. F. Jensen, and M. A. Schmidt, *J. Microelectromechanical Syst.* **1998**, *7*, 128.

[74] S. Enoch, G. Tayeb, P. Sabouroux, N. Guérin, and P. Vincent, *Phys. Rev. Lett.* **2002**, *89*, 213902.

[75] J. K. Gansel, M. Thiel, M. S. Rill, M. Decker, K. Bade, V. Saile, G. von Freymann, S. Linden, and M. Wegener, *Science* **2009**, *325*, 1513.

[76] P. Li, B. Liu, Y. Ni, K. K. Liew, J. Sze, S. Chen, and S. Shen, *Adv. Mater.* **2015**, n/a.

[77] G. Smith, A. Gentle, M. Arnold, and M. Cortie, *Nanophotonics* **2016**, *5*, .

[78] E. B. Franke, C. L. Trimble, J. S. Hale, M. Schubert, and J. A. Woollam, *Appl. Phys. Lett.* **2000**, *77*, 930.

[79] T. Inoue, M. De Zoysa, T. Asano, and S. Noda, *Nat. Mater.* **2014**, *13*, 928.

[80] S. Vassant, I. Moldovan Doyen, F. Marquier, F. Pardo, U. Gennser, A. Cavanna, J. L. Pelouard, and J. J. Greffet, *Appl. Phys. Lett.* **2013**, *102*, 81125.

[81] V. W. Brar, M. C. Sherrott, M. S. Jang, S. Kim, L. Kim, M. Choi, L. A. Sweatlock, and H. A. Atwater, *Nat. Commun.* **2015**, *6*, 7032.

[82] M. A. Kats, R. Blanchard, S. Zhang, P. Genevet, C. Ko, S. Ramanathan, and F. Capasso, *Phys. Rev. X* **2014**, *3*, 1.

[83] L. Xiao, H. Ma, J. Liu, W. Zhao, Y. Jia, Q. Zhao, K. Liu, Y. Wu, Y. Wei, S. Fan, and K. Jiang, *Nano Lett.* **2015**, *15*, 8365.

[84] L. Phan, W. G. Walkup IV, D. D. Ordinario, E. Karshalev, J. M. Jocson, A. M. Burke, and A. A. Gorodetsky, *Adv. Mater.* **2013**, *25*, 5621.

[85] T. Han, X. Bai, J. T. L. Thong, B. Li, and C. W. Qiu, *Adv. Mater.* **2014**, *26*, 1731.

[86] Z. Miao, Q. Wu, X. Li, Q. He, K. Ding, Z. An, Y. Zhang, and L. Zhou, *Phys. Rev. X* **2015**, *5*, 1.

[87] S. Fan, W. Suh, and J. D. Joannopoulos, *J. Opt. Soc. Am. A* **2003**, *20*, 569.

[88] N. Kinsey, C. DeVault, J. Kim, M. Ferrera, V. M. Shalaev, and A. Boltasseva, *Optica* **2015**, *2*, 616.

[89] H.-T. Chen, W. J. Padilla, J. M. O. Zide, S. R. Bank, A. C. Gossard, A. J. Taylor, and R. D. Averitt, *Opt. Lett.* **2007**, *32*, 1620.

[90] C. Jagadish and S. Pearton, Eds., *Zinc Oxide Bulk, Thin Films and Nanostructures*, Elsevier, Oxford, **2006**.

[91] P. Sharma, K. Sreenivas, and K. V. Rao, *J. Appl. Phys.* **2003**, *93*, 3963.

[92] T. L. Tansley and D. F. Neely, *Thin Solid Films* **1984**, *121*, 95.

[93] D. H. Zhang, *Mater. Chem. Phys.* **1996**, *45*, 248.

[94] A. T. Vai, N. Rashidi, Y. Fang, V. L. Kuznetsov, and P. P. Edwards, *J. Phys. Condens. Matter* **2016**, *28*, 224003.

[95] K. Liu, M. Sakurai, M. Liao, and M. Aono, *J. Phys. Chem. C* **2010**, *114*, 19835.

[96] W. Streyer, S. Law, G. Rooney, T. Jacobs, and D. Wasserman, *Opt. Express* **2013**, *21*, 9113.

[97] H. K. Yadav and V. Gupta, *J. Appl. Phys.* **2012**, *111*, 0.

[98] C. Chen, H. He, Y. Lu, K. Wu, and Z. Ye, *ACS Appl. Mater. Interfaces* **2013**, *5*, 6354.

[99] B. L. Zhu, J. Wang, S. J. Zhu, J. Wu, R. Wu, D. W. Zeng, and C. S. Xie, *Thin Solid Films* **2011**, *519*, 3809.

[100] J. C. Moore and C. V. Thompson, *Sensors* **2013**, *13*, 9921.

[101] P. K. Shrestha, Y. T. Chun, and D. Chu, *Light Sci. Appl.* **2015**, *4*, .

[102] M. G. Pitt, R. W. Zehner, K. R. Amudson, and H. Gates, in *SID Symposium Digest Technical Papers*, **2002**, 1378.

[103] M. R. Fernández, E. Z. Casanova, and I. G. Alonso, *Sustainability* **2015**, *7*, 10854.

[104] K. Xiong, G. Emilsson, A. Maziz, X. Yang, L. Shao, E. W. H. Jager, and A. B. Dahlin, *Adv. Mater.* **2016**, *28*, 9956.

[105] M. Keshavarz Hedayati and M. Elbahri, *Plasmonics* **2016**, 1.

[106] M. Miyata, H. Hatada, and J. Takahara, *Nano Lett.* **2016**, *16*, 3166.

[107] X. Zhu, C. Vannahme, E. Højlund-Nielsen, N. A. Mortensen, and A. Kristensen, *Nat. Nanotechnol.* **2015**, *11*, 325.

[108] K. Kumar, H. Duan, R. S. Hegde, S. C. W. Koh, J. N. Wei, and J. K. W. Yang, *Nat. Nanotechnol.* **2012**, *7*, 557.

[109] A. S. Roberts, A. Pors, O. Albrektsen, and S. I. Bozhevolnyi, *Nano Lett.* **2014**, *14*, 783.

[110] S. J. Tan, L. Zhang, D. Zhu, X. M. Goh, Y. M. Wang, K. Kumar, C. W. Qiu, and J. K. W. Yang, *Nano Lett.* **2014**, *14*, 4023.

[111] X. Duan, S. Kamin, and N. Liu, *Nat. Commun.* **2017**, *8*, 1.

[112] A. Tsuboi, K. Nakamura, and N. Kobayashi, *Adv. Mater.* **2013**, *25*, 3197.

[113] G. Wang, X. Chen, S. Liu, C. Wong, and S. Chu, *ACS Nano* **2016**, *10*, 1788.

[114] A. Tsuboi, K. Nakamura, and N. Kobayashi, *Chem. Mater.* **2014**, *26*, 6477.

[115] A. P. Cohn, K. Share, R. Carter, L. Oakes, and C. L. Pint, *Nano Lett.* **2016**, *16*, 543.

[116] T. D. James, P. Mulvaney, and A. Roberts, *Nano Lett.* **2016**, *16*, 3817.

[117] Z. J. Coppens, I. I. Kravchenko, and J. G. Valentine, *Adv. Opt. Mater.* **2016**, *4*, 671.

[118] Z. J. Coppens and J. G. Valentine, *Adv. Mater.* **2017**, *1701275*, 1.

[119] Z. Q. Li, E. A. Henriksen, Z. Jiang, Z. Hao, M. C. Martin, P. Kim, H. L. Stormer, and D. N. Basov, *Nat. Phys.* **2008**, *4*, 532.

[120] F. Wang, Y. Zhang, C. Tian, C. Girit, A. Zettl, M. Crommie, and Y. R. Shen, *Science* **2008**, *320*, 206.

[121] M. S. D. and J. K. Alfonso Reina, Xiaoting Jia, John Ho, Daniel Nezich, Hyungbin Son, Vladimir Bulovic, *Nano Lett.* **2009**, *9*, 30.

[122] J. Pu, L. Tang, C. Li, T. Li, L. Ling, K. Zhang, Q. Li, and Y. Yao, *RSC Adv.* **2015**, *5*, 44142.

[123] P. Hsu, X. Liu, C. Liu, X. Xie, H. R. Lee, A. J. Welch, and T. Zhao, *Nano Lett.* **2014**, *15*, 365.

[124] J. K. Tong, X. Huang, S. V. Boriskina, J. Loomis, Y. Xu, and G. Chen, *ACS Photonics* **2015**, *2*, 769.

[125] P.-C. Hsu, A. Y. Song, P. B. Catrysse, C. Liu, Y. Peng, J. Xie, S. Fan, and Y. Cui, *Science* **2016**, *353*, 1019.

[126] R. Aaswath, A. Marc, Z. Linxiao, E. Rephaeli, and S. Fan, *Nature* **2014**, *515*, 540.

[127] W. Li, Z. J. Coppens, L. V. Besteiro, W. Wang, A. O. Govorov, and J. Valentine, *Nat. Commun.* **2015**, *6*, 8379.

[128] N. Liu, M. Mesch, T. Weiss, M. Hentschel, and H. Giessen, *Nano Lett.* **2010**, *10*, 2342.

[129] W. Lee and S. S. S.-J. S. S. Park, *Chem. Rev.* **2014**, *114*, 7487.

[130] P. Moitra, B. A. Slovick, W. Li, I. I. Kravchencko, D. P. Briggs, S. Krishnamurthy, and J. Valentine, *ACS Photonics* **2015**, *2*, 692.

[131] L. J. Guo, *Adv. Mater.* **2007**, *19*, 495.